Article:
Schantl, P, Hauzenberger, C, Finger, F et al. (2019) New evidence for the prograde and retrograde PT-path of high-pressure granulites, Moldanubian Zone, Lower Austria, by Zr-in-rutile thermometry and garnet diffusion modelling. Lithos, 342-343. pp. 420-439. ISSN: 0024-4937

https://doi.org/10.1016/j.lithos.2019.05.041

New evidence for the prograde and retrograde PT-path of high-pressure granulites, Moldanubian Zone, Lower Austria, by Zr-in-rutile thermometry and garnet diffusion modelling

Philip Schantl [a,*], Christoph Hauzenberger [a], Friedrich Finger [b] Thomas Müller [c], Manfred Linner [d],

[a] Department of Petrology and Geochemistry, NAWI Graz Geocenter, University of Graz, Universitätsplatz 2, 8010, Graz, Austria

[b] Department of Chemistry and Physics of Materials, University of Salzburg, Jakob-Haringer-Strasse 2a, 5020, Salzburg, Austria

[c] School of Earth and Environment, University of Leeds, Maths/Earth and Environment Building, Leeds, LS2 9JT, United Kingdom

[d] Department of Hard Rock Geology, Geological Survey of Austria, Neulinggasse 38, 1030, Vienna, Austria

*Corresponding author.

Telephone: +43 (0)316 380 5543.

E-mail address: philip.schantl@uni-graz.at (P. Schantl)

ABSTRACT

Compositional zoning in garnet, mineral inclusions and the application of the Zr-in-rutile thermometry on rutile inclusions in garnet in combination with conventional geothermobarometry and thermodynamic modelling allows a reconstruction of the prograde pressure-temperature evolution in felsic and mafic high-pressure granulites from the Moldanubian Zone, Bohemian Massif, Lower Austria. Most garnets in these rocks show homogeneous core compositions with high grossular contents (~30 mol.%), while their rim zones have a markedly reduced grossular content. Rutile inclusions in the grossular rich garnet cores have low Zr concentrations (400 to 1300 ppm) indicating a formation temperature of ~810–820 °C which implies that the garnet host grew at these temperature conditions as well. Based on numerous polycrystalline melt inclusions, high Ti-biotite relics and a generally high Ti concentration in garnet cores, the peritectic biotite breakdown reaction is considered to be responsible for a first garnet growth, now observed as high-grossular garnet cores. The corresponding pressure is estimated to be in the range of 1.6 to 2.5 GPa, based on experimentally determined biotite breakdown reactions, thermodynamic modelling and the occurrence of high-Ti biotite in garnet cores. Rutile inclusions in low-Ca garnet rims contain significantly higher Zr concentrations (1700 to 5800 ppm) resulting in ultrahigh temperatures of ~1030 °C. Similar temperature as well as corresponding pressure estimates of 1000 ± 50 °C and 1.60 ± 0.10 GPa were obtained by geothermobarometry and thermodynamic modelling using garnet rim and re-integrated ternary feldspar compositions. These high pressure and ultrahigh temperature conditions are well known from literature for these granulites. The proposed two-phase garnet growth is not only seen in different temperatures obtained from rutile inclusions in garnet core and rim areas, but also in discontinuous trace (Cr, Ga, P, Ti, V, Zr) and heavy rare earth element profiles across garnet porphyroblasts, implying a different reaction mechanism for garnet rim growth. This second phase of garnet growth must have occurred during near isobaric heating to the ultrahigh temperature peak, most likely even at slightly lower pressures compared to the garnet core growth.

By applying a binary Fe-Mg diffusion model to strongly zoned garnet grains a maximum timescale of 5–6 million years was estimated for the exhumation and cooling process, assuming a linear cooling path from 1000 °C at 1.6 GPa to 760 °C at 0.8 GPa. This short-lived ultrahigh temperature event corresponds to cooling and exhumation rates of 40–50 °C Ma^{-1} and 5.3–6.6 mm y^{-1}, respectively.

Keywords: Bohemian Massif; Moldanubian granulite; prograde metamorphic evolution; Zr-in-rutile thermometry; rapid exhumation/cooling

1. INTRODUCTION

Ultrahigh-temperature (UHT) metamorphism is defined as a sub-division of the granulite facies (700–1000 °C and 0.3–1.5 GPa) where rocks are subjected to extreme temperatures of more than 900 °C (Harley, 1998). More than forty occurrences of UHT rocks have been documented so far, for instance in the Highland Complex in Sri Lanka (e.g. Osanai et al., 2006), the Oygarden Complex in Antarctica (Kelly and Harley, 2004), the Labwor Hills in Uganda (Sandiford et al., 1987), the Lewisian Complex in Scotland (Baba, 2003), the Gruf Complex in Italy (Droop and Bucher-Nurminen, 1984), the Peekskill, New York, USA (Caporuscio and Morse, 1978), the Saxonian Granulite Massif (Rötzler and Romer, 2001; O'Brien and Rötzler, 2003) and the Moldanubian Zone of the Bohemian Massif in Austria and the Czech Republic (Carswell and O'Brien, 1993; Kotková and Harley, 1999; Cooke, 2000; Cooke et al. 2000; Janousek et al., 2004; Vrána et al., 2005).

Studying the petrogenesis and the geological (tectonic) evolution of UHT rocks is a challenge, due to the fact that high peak temperatures erase nearly all traces of the incipient metamorphic PT path (e.g. Carswell and O'Brien, 1993; Hauzenberger et al., 2005; Jedlička et al., 2015). The rapid reaction kinetics at high temperatures causes most pre-UHT mineral phases to decompose and even stable minerals like garnet re-equilibrate by solid state diffusion where chemical zoning pattern as a consequence of prograde growth is erased. Only in case of a short residence time at high peak conditions, and in a fluid/melt poor environment, there is a chance that minerals from the prograde metamorphic stage survive. For instance, Cooke et al. (2000) documented the preservation of early, prograde high-Ca garnet cores surrounded by high-Mg garnet mantle and Zack et al. (2004) and Usuki et al. (2017) showed that Zr-in-rutile thermometry gives meaningful results for prograde rutile relics in garnet.

The focus of this study are felsic to mafic UHT granulites from the Austrian part of the Bohemian Massif. The high-grade metamorphic nature of these rocks was recognized many years

88 ago (Scharbert and Kurat, 1974). Later work by Carswell and O'Brien (1993), Cooke et al. (2000)
89 and Cooke (2000) has highlighted a very complex polyphase PTt (pressure-temperature-time)
90 evolution of these rocks, involving a HP-HT (high-pressure and high-temperature) granulite facies
91 stage (~1000 °C and ~1.6 GPa), subsequent near isothermal decompression to intermediate
92 granulite facies conditions (900 °C, 1.0 GPa), and final cooling to amphibolite facies conditions
93 with significantly lower exhumations rates.
94 More recently Faryad et al. (2010) postulated that granulites in the Bohemian Massif
95 experienced an eclogite facies PT-path prior to the HP-HT granulite facies stage. Based on coesite
96 and microdiamond inclusions in garnets, Perraki and Faryad (2014) reported UHP metamorphic
97 conditions of about 3.2–4.0 GPa (at 700 °C) for granulites in the Czech part of the Bohemian
98 Massif. Whether the granulites in the Austrian part of the Moldanubian Zone experienced a similar
99 eclogite facies prograde metamorphic evolution, is controversially debated. Carswell and O'Brien
100 (1993) argued that an eclogite facies imprint on these rocks is unlikely due to the lack of clear
101 eclogite facies textures and mineral assemblages in metabasic rocks directly enclosed within these
102 granulites.
103 In this study, we present new evidence for the prograde evolution of the Moldanubian
104 granulites from the Pöchlarn-Wieselburg, Dunkelsteinerwald and Zöbing areas, Lower Austria,
105 based on major and trace element zoning patterns of garnets, and by investigating the inclusions
106 preserved in the garnets, with particular emphasis on Zr-in-rutile thermometry. In addition, we
107 model the retrograde Fe-Mg diffusive re-equilibration of garnet based on detailed microprobe
108 profiles to quantify the fast exhumation and cooling segment of the retrograde path.
109
110 **2. REGIONAL GEOLOGY**
111
112 The Variscan orogenic belt is exposed in several large-scale basement blocks which outcrop
113 across western and central Europe (Fig. 1a). The Bohemian Massif is the easternmost of these

Variscan basement blocks. The Austrian sector of the Bohemian Massif exposes mainly the Moldanubian Zone, which is considered to represent the exhumed core of the Variscan orogeny. Regionally, the Moldanubian Zone is subdivided into three tectonic units, the hangingwall Gföhl Unit, the underlying Drosendorf Unit (Variegated Series) and the Ostrong Unit (Monotonous Series) at the bottom (e.g. Fuchs and Matura, 1968). The UHT granulites are part of the Gföhl Unit, and occur in contact to large masses of migmatic gneiss termed the Gföhl gneiss. There is wide agreement that the Gföhl Unit underwent Variscan continental collision and, subsequently, fast exhumation to mid-crustal levels (Finger et al. 2007).

The Moldanubian granulites in Lower Austria show significant similarities in terms of lithology and metamorphism to their counterparts in the Czech Republic, which have been more intensively studied in the recent past (e.g. Faryad, 2009; Faryad et al., 2010; Jedlička et al., 2015; Usuki et al., 2017). Almost all Moldanubian granulite bodies contain both felsic and mafic types, with estimated peak metamorphic conditions ranging between 850–1100 °C and 1.6–2.0 GPa (e.g. Carswell and O'Brien, 1993; Petrakakis 1997; O'Brien et al., 1997; Kotková and Harley, 1999; Cooke, 2000; Cooke et al., 2000; Cooke and O'Brien, 2001; Štípská and Powell, 2005; Tajčmanová, et al., 2006; Kotková and Harley, 2010).

U-Pb zircon and Rb-Sr whole rock dating show two distinct age clusters at 490–430 Ma and c. 340 Ma (Arnold and Scharbert, 1973; Frank et al., 1990; Kröner et al., 2000; Friedl et al., 2004, 2011). The Ordovician ages are generally interpreted as the time of protolith formation, the early Carboniferous dates as the age of the UHT stage of metamorphism. A number of ages of around 370 Ma, obtained by Sm-Nd garnet geochronology in various granulites and peridotites (Carswell and Jamtveit, 1990; Brückner et al., 1991; Prince et al., 2000) are interpreted to reflect a Devonian HP-UHP event.

3. METHODS

Quantitative mineral analyses were performed on carbon coated thin sections using a JEOL JSM 6310 scanning electron microscope (SEM) at the NAWI Graz Geocenter-Department of Petrology and Geochemistry, University of Graz, Austria equipped with a LINK ISIS energy dispersive system and a MICROSPEC wavelength dispersive system. Additional analyses and chemical maps were obtained using a JEOL JXA-8200 electron probe microanalyzer (EPMA) at the Eugen F. Stumpfl Electron Microprobe Laboratory, UZAG, University of Leoben, University of Graz, Graz University of Technology. BSE images of submicron mineral inclusions were obtained with a JEOL JXA-8530F Plus EPMA at the NAWI Graz Geocenter. Measurement conditions of the SEM and EPMA were 15kV acceleration voltage, 10 nA beam current and ~1 µm beam diameter with 20s counting time on peak and 10s on each background.

To ensure that the garnets selected in thin section for compositional profiles have actually been cut through their true cores, we measured the average garnet grain size as seen in the related hand specimen and then chose equivalent sized garnets in the thin section for analysis.

Detailed systematic investigation of mineral inclusions in garnet, zircon and kyanite was conducted using polished thin sections of whole rocks and separated grains embedded in epoxy. More than 700 garnet, zircon and kyanite grains from different granulite samples were investigated. In order to obtain central cuts through the separated garnet, kyanite and zircon grains only the largest were selected and ground down until their predetermined maximum diameter was reached.

Concentration of Zr-in-rutile was determined using the EPMA with operating conditions of 15kV, 120nA beam current, ~1 µm beam diameter and count times of 60s on peak and 30s on each background. So as to enhance the detection limit, three spectrometers equipped with TAP and PETJ analyzer crystals were chosen to measure the Zr-La ratio. For the trace element Zr-in-rutile thermometer we used the empirically calibration of Zack et al. (2004) as well as the experimentally calibration of Ferry and Watson (2007) and Tomkins et al. (2007).

The original composition of the early, peak hypersolvus ternary feldspar was determined by the re-integration technique of Raase (1998). Following this procedure the host and exsolution

166 feldspar were analyzed by a slightly defocused microprobe beam to avoid Na loss. The volume
167 percentage of the exsolved phase was determined by computer image analysis of back-scattered-
168 electron (BSE) images and then transformed into weight percentages. The bulk composition of the
169 early, peak hypersolvus ternary feldspar was obtained by combining the weight percentages of both
170 the host and exsolution feldspar phases.

171 Whole rock compositions were determined by X-ray fluorescence (XRF) on glassy discs
172 using a Bruker Pioneer S4 under standard conditions at the NAWI Graz Geocentre.

173 Trace elements and REE contents in garnet, apatite and perthitic alkali-feldspar were
174 obtained from polished thin sections using an LA ICP MS (laser ablation inductively coupled
175 plasma mass spectrometer) system at the NAWI Graz Central Lab for Water, Minerals and Rocks,
176 with an ESI New Wave 193 Excimer Laser (193nm wavelength) coupled to an quadrupole Agilent
177 7500 CX mass spectrometer. The settings for the element analyses were a beam size of 35–50 µm,
178 with a fluence energy of ~4–5 J/cm^2, helium flow of 0.7 l/min, 30 ms gas blank followed by 60 s of
179 ablation and a dwell time of 30 s for each mass were used for the element analyses. We used NIST
180 SRM 612 glass for standardization. As internal calibration Si and Ca were used for garnet, perthitic
181 alkali-feldspar and apatite, repsectively. The USGS reference glass BCR-2G was analyzed as a
182 monitor standard that could be reproduced within errors. Values of 0.1–0.5 ppm were quantified
183 fairly accurate. For data reduction, the software "GLITTER" was used and the values for NIST
184 SRM 612 were taken from Jochum et al. (2011).

185 Mineral abbreviations used in subsequent sections of this paper are after Whitney and Evans
186 (2010).

187

188 **4. PETROGRAPHY AND MINERAL CHEMISTRY**

189

190 For this study, 225 granulite samples were collected from 62 localities within three granulite
191 bodies in the south-easternmost Moldanubian Zone in Lower Austria. All three granulite bodies

192 formed a coherent granulite occurrence, which is now displaced by the Diendorf Fault system. (21
193 samples from Zöbing, 101 samples from Dunkelsteinerwald and 103 samples from Pöchlarn-
194 Wieselburg). The sample localities are shown in Figure 1b, with geographical coordinates,
195 lithologies etc. provided in Table A of the supplementary material.
196 The detailed petrography and textural relations of the Moldanubian granulites in Lower
197 Austria, have been discussed in Carswell and O'Brien (1993), Cooke et al. (2000) and Cooke
198 (2000). Two varieties of granulites are present. The most abundant type is a middle to fine-grained,
199 leucocratic granulite. With the exception of the small granulite body near Zöbing, these felsic
200 granulites are accompanied by subordinate, massive, mafic granulites. Both rock types are acidic in
201 terms of their SiO_2 content but differ in their absolute concentrations. Whilst felsic granulites show
202 70–77 wt.% SiO_2, mafic granulites are lower with 63–70 wt.%. In addition, mafic granulites are
203 enriched in CaO, FeO, MgO and depleted in K_2O resulting in a different HP mineral assemblage
204 (e.g. Fiala et al. 1987; Carswell and O'Brien, 1993).
205
206 **4.1 Felsic granulites**
207
208 The retained HP granulite facies mineral assemblage in felsic granulites is represented by
209 garnet + kyanite + perthitic alkali-feldspar + quartz, along with accessory rutile, apatite and zircon.
210 This equilibrium assemblage is best preserved in least deformed, very light-coloured samples with
211 partly preserved granoblastic fabrics (Fig. 2a). Red garnet, deep-blue kyanite and perthitic alkali-
212 feldspar, reaching up to 3 mm in size, appear as disseminated coarser grained porphyroblasts
213 enclosed in a strongly recrystallized quartzo-feldspatic matrix (Fig. 2b).
214 Retrogression accompanied by strong deformation has led to the formation of secondary
215 biotite, sillimanite, ilmenite and recrystallization of the early single-phase perthitic alkali-feldspar
216 into separate K-feldspar and plagioclase. In addition, fine-grained plagioclase (100–300 µm in size)
217 within the matrix appear to have formed due to the recrystallization of the early feldspar. Retrograde

biotite predominately occurs within distinct slightly darker bands developed within the very light-coloured felsic granulite (Fig. 2c). Within these bands, fine-grained sillimanite interpenetrates the flaky biotite and rare ilmenite to form elongated masses oriented parallel to foliation, which is mainly defined by quartz ribbons (Fig. 2d, e). The formation of sillimanite and biotite is the result of the continuous reaction garnet + K-feldspar + H_2O = biotite + sillimanite + quartz. Locally, some sillimanite seems to have been formed by direct replacement of earlier kyanite.

Garnets

Light red, subhedral garnet porphyroblasts show two different patterns of chemical zoning. Garnet zoning profile type I (Fig. 3a, b and c) appears in felsic granulites with a whole rock composition slightly elevated in CaO (1.80–3.60 wt.%). Their core regions (up to c. 800 µm wide) are homogeneous with a compositional of $Alm_{41–48}$, $Pyp_{22–27}$, $Grs_{24–36}$ and Sps_{1} (Table 1). In contrary, their rims (up to c. 500 µm wide) with $Alm_{46–57}$, $Pyp_{24–34}$, $Grs_{7–28}$ Sps_{1} show a marked chemical zonation, where grossular content decreases substantially, matched by an increase in almandine and pyrope as well as an increase in X_{Mg}. The spessartine content remains constant along the whole profile. A similar garnet zoning pattern has been reported from leucocratic granulites in the Blanský les Massif, Czech Republic (Kotková and Harley, 2010).

Garnet zoning profile type II (Fig. 3d and e) usually occurs in felsic granulites with slightly lower amounts of CaO 0.60–1.20 wt.% in their whole rock geochemistry. The garnet has a composition in the range of $Alm_{78–46}$, $Pyp_{44–16}$, $Grs_{4–14}$ and $Sps_{1–2}$ (Table 1) and is characterized by the absence of a wide, homogeneous core. The zonation is also less pronounced with grossular content decreasing gradually from core to the rims, while almandine and pyrope contents increase progressively from core towards the rims. Spessartine content is low throughout the garnet with no obvious zoning.

Small garnet grains in biotite and sillimanite rich domains (Fig. 2d, e) have a general composition of Alm_{77}, Pyp_{17}, Grs_{4} and Sps_{1} (Table 1).

Feldspars

Carswell and O'Brien (1993) and O'Brien and Rötzler (2003) documented the occurrence of perthitic alkali-feldspar instead of an early peak ternary feldspar in felsic granulites in the Moldanubian Zone. This perthitic alkali-feldspar recrystallized into K-feldspar and plagioclase during retrogression. Compositional re-integration of the millimeter-sized, perthitic alkali-feldspar porphyroblasts reveals a composition in the range of $An_{5–11}$ $Ab_{17–25}$ $Or_{78–64}$ in our samples (Table 3).

Significantly finer-grained plagioclase (100 to 300 µm in size) within the quartz-rich granoblastic matrix is also interpreted to be the result of recrystallization of the early single-phase feldspar. It has a compositional range between An_{17} Ab_{80} to An_{24} Ab_{75} (Table 4).

Biotites

Biotite, up to 1.5 mm in length, is especially abundant within the slightly darker bands, which pervade the leucocratic granulites (Fig. 2c, d). These biotite flakes have a significant fluorine content, with a maximum of 5.40 wt.% (1.265 apfu) (Table 2). Rare biotites outside the slightly darker bands also show elevated F contents, typically higher than 0.5 wt.%, as reported from similar rocks by Tropper and Hauzenberger (2015).

4.2 Mafic granulites

Mafic granulites (Fig. 2f) are not as common as the felsic type. In some places a sharp boundary between both granulites is observed, in other cases gradual changes are noticed (e.g. road outcrop between Aggsbach-Dorf and Wolfstein, E15.423122, N48.292625). The HP granulite facies mineral assemblage is represented by the coexistence of garnet + clinopyroxene + ternary feldspar + quartz, together with accessory rutile, apatite and zircon (Fig. 2g). However, clinopyroxene is not observed as stable phase in the matrix anymore and is only found as inclusion in garnet. Red garnet and antiperthitic plagioclase form homogeneously distributed coarser grains of up to 1.5 mm size,

which are embedded within a recrystallized fine-grained quartzo-feldspathic matrix. Almost all samples of mafic granulites display an intensive retrogression accompanied with the growth of abundant orthopyroxene (Fig. 2g). These orthopyroxene grains were formed during decompression subsequent to the HP granulite facies peak (Cooke, 2000).

In some samples the retrogression and rehydration cause the growth of late stage biotite and amphibole which are locally intergrown with orthopyroxene, small ilmenite and garnet grains (Fig. 2i, j). The formation of these amphibole and biotite grains is due to a garnet and/or orthopyroxene consuming reaction. As a consequence of retrogression, the former single high-temperature feldspar phase recrystallized into antiperthitic plagioclase with irregular intergrowths between plagioclase host (80–74 vol.%) and K-feldspar patches. Fine-grained plagioclase and minor K-feldspar within the matrix are also thought to be formed by recrystallization of the early single-phase peak feldspar and are considered to be part of the retrograde metamorphic assemblage.

Garnets

Large garnet porphyroblasts in mafic granulites (Fig. 3f) display a garnet zonation pattern similar to the garnet zonation profile type I seen in felsic granulites. The zonation is characterized by a uniform central high grossular portion (up to 1 mm wide) with a narrow compositional range of $Alm_{43–46}$ $Pyp_{14–16}$ $Grs_{39–41}$ Sps_{1} (Table 1). In contrast, their rims (up to 200 µm wide) are strongly zoned with a grossular decrease and pyrope and almandine increase. Their composition is $Alm_{44–59}$ $Pyp_{19–28}$ $Grs_{10–36}$ $Sps_{1–2}$. In some garnets, an increase of X_{Mg} at the rim zone is also present. Within the mafic granulites there is always a slight increase in the spessartine content towards the rims of garnets, typical for resorption and back diffusion (Müller et al., 2015). Small garnet grains associated with amphibole, biotite and ilmenite rich patches in some mafic granulites are Alm_{63} Pyp_{19} Grs_{16} Sps_{2} (Table 1).

Feldspars

296 Coarse grained porphyroblasts (up to 1.5 mm size) of antiperthitic plagioclase occur in a
297 strongly recrystallized, granoblastic matrix. They show an irregular, patchy-like intergrowth
298 between host and exsolution lamellae, with a calculated re-integrated composition of An_{39} Ab_{35} Or_{26}
299 (Table 3). Recrystallized fine-grained matrix plagioclase and K-feldspar (200 to 300 μm in size),
300 coexisting with the retrograde mineral assemblage of amphibole + biotite + ilmenite, show
301 compositions about An_{27} Ab_{71} and Or_{89} Ab_{10} (Table 3 and 4), respectively.
302
303 ***Orthopyroxenes***
304 Numerous small orthopyroxene grains belonging to the retrograded mineral assemblage
305 occur throughout the rock matrix in mafic granulites (Fig. 2i). Orthopyroxene is rich in ferrosilite
306 component (X_{Mg} 0.43–0.22), with Al_2O_3 content of about 0.44–1.19 wt.% (Table 2).
307
308 ***Amphiboles***
309 Light to dark green secondary amphiboles, up to 600 μm in size, occur primarily in biotite
310 and ilmenite rich mafic granulites, which are strongly affected by retrogression. They are Ferro-
311 Tschermakites, with low fluorine and chlorine contents (~0.05 wt.%, Cl ~0.35 wt.%, respectively)
312 and X_{Mg} values ranging between 0.41 and 0.44 (Table 2).
313
314 ***Biotites***
315 Retrograde biotites (up to 500 μm in size) are especially abundant within amphibole and
316 ilmenite rich domains (Fig. 2j). They have TiO_2 contents of ~4.34 wt.%, X_{Mg} values of 0.44 and,
317 compared with biotites in felsic granulites, have low fluorine contents (<0.50 wt.% / <0.116 apfu)
318 (Table 2).
319
320 **5. MINERAL INCLUSIONS**
321

Red garnet pophyroblasts from both, felsic and mafic granulites commonly enclose a variety of different mineral phases. The most common inclusions are quartz, perthitic alkali-feldspar, antiperthitic plagioclase, kyanite, apatite and rutile. However, white mica relics, clinopyroxene, high-Ti biotite, and polyphase mineral inclusions composed of quartz + K-feldspar + plagioclase or kaolinite + K-feldspar + quartz are also present in some garnet grains. Deep blue kyanite porpyhroblasts in felsic granulites contain perthitic alkali-feldpsar. K-feldspar, quartz, monazite and pyrite grains have been observed within zircon grains.

We distinguish two different varieties of rutile inclusions within garnets. The first type forms thin, euhedral needles, with greater abundance in garnet cores compared to their rims. This needle-like rutile clearly indicates exsolution along crystallographic planes from a former high titanium garnet during retrogression. The second type of rutile inclusions form rounded, anhedral grains, up to 300 µm in size (Fig. 4a) which are very common in both, the cores and rims of garnet.

Apatite is a common inclusion within garnets of both felsic and mafic granulites. It appears as a prismatic subhedral single phase up to 300 µm in size and is present in the core as well as the rim of the garnet.

Euhedral biotite inclusions, up to 40 µm in size, are only found in the grossular-rich cores of garnet from felsic granulites, in some cases associated with tiny rutile and quartz (Fig. 4b). These biotites have very high TiO_2 content (6.1 wt.%) and elevated fluorine content (2.32 wt. %) (Table 2).

Perthitic alkali-feldspar, up to a maximum size of ~400 µm, are commonly included within both garnets and kyanites of the felsic granulites (Fig. 4c). The perthitic texture is laminar, with plagioclase exsolution occupying 30–35 vol.% of the K-feldspar host. The reintegrated compositions are similar to those of matrix perthite grains, approximately An_6 Ab_{26} Or_{68} (Table 3). In contrast, garnets of mafic granulites contain antiperthitic plagioclase inclusions.

Clinopyroxene inclusions, up to 80 µm in size, are found in the medium to low Ca garnet zone in mafic granulites (Fig. 4d). It has a diopsidic composition with X_{Mg} = 0.55–0.61, X_{Na} =

Na/(Na+Ca) = 0.04–0.05 and Al^{IV} = 0.015–0.024 (Table 1). The complete lack of clinopyroxene in the matrix and the abundant occurrence of orthopyroxene indicates that the decompression driven reaction grt + cpx + qz = opx + pl took place.

White mica occurs in polyphase inclusions within the high-grossular garnet cores, intergrown with biotite, quartz and locally also with apatite and rutile (Fig. 4e). Although these inclusions show some signs of late alteration, analyses of white mica reveal a phengitic composition with MgO contents of 0.90–1.44 wt.%, and FeO of 1.68–2.47 wt.%, and a Si content of up to 3.164 apfu (Table 2). Biotite in such inclusions has an unusual low TiO_2 content of about 0.30 wt.%.

Intergrowths of anhedral kaolinite, K-feldspar and quartz were found in the central parts of Ca-rich garnets from felsic granulites (Fig. 4f). These inclusions reach up to a maximum of 300 µm in size and frequently contain kyanite, tiny rutile and small flakes of strongly decomposed white mica.

Small euhedral-shaped, former melt inclusions in crack-free garnet domains (Fig. 4g–i) consist of quartz, K-feldspar, biotite, ± rutile, ± plagioclase, ± ilmenite and ± apatite. This type of inclusion is commonly found in felsic and mafic granulites within the garnet core and rim.

6. GARNET TRACE ELEMENT ZONING

The garnet from felsic granulite sample WG336 was selected to compare major and trace element zoning (Fig. 3a and 5). In this particular garnet the zoning pattern of trace elements is correlated to changes in grossular, almandine and pyrope contents. However, the decrease or increase in trace elements occurs over a shorter distance compared to the major elements. Therefore, the slower diffusing trace elements such as Ti, Zr, Y and Er are better suitable to define the original core-rim interface (Fig. 5). For detailed LA-ICP-MS mineral chemical data see Table B in the supplementary material. The selected garnet shows a general homogeneous core composition, rich in phosphorous, titanium and zirconium, with a marked and sharp decrease of these elements at

the outer rims. The distribution of vanadium, chromium and gallium follows the opposite trend, with low concentrations in the core and high concentrations at the rims (Fig. 5). Yttrium, as well as heavy REE (HREE: erbium, ytterbium) show a relatively uniform concentration in the garnet core, with a marked depletion at the outermost rim. Light REE (LREE: neodymium, europium) concentrations are generally low with flat profiles in the core and strong depletion towards the rims. In a chondrite normalized spider plot (Fig. 5q), using chondrite REE compositions from Nakamura (1974), this particular garnet shows HREE-enriched and steep LREE-depleted pattern for the core as well as for the rim. Furthermore, the rim composition is even more depleted in REE compared to the core. It also has a negative europium anomaly as a whole, which is more pronounced for rim composition.

7. APATITE TRACE ELEMENT COMPOSITION

Fourteen single apatite grains with different textural appearance have been analysed for trace elements from the same felsic granulite sample WG336. LA-ICP-MS mineral chemical data are given in Table C in the supplementary material. Interestingly, apatite crystals cannot only be differentiated based on their textural appearance but also on their varying Y concentrations. Apatite within the high-grossular core of garnet shows by far the lowest Y concentrations (310–530 ppm, mean=425, n=4). In contrast, apatite within the garnet rim (967–1003 ppm, mean=985, n=2) and matrix (649–862 ppm, mean= 765, n=8) are significantly higher in Y. Based on the chondrite normalized spider plot in Fig. 6a, all analysed apatite crystals show a steep HREE depleted and LREE-enriched pattern with a marked negative Eu anomaly. Apatite within the garnet core is more depleted in HREE compared to those in the matrix and garnet rim area.

8. PERTHITIC ALKALI-FELDSPAR TRACE ELEMENT COMPOSITION

Nine spot analyses by LA-ICP-MS on large perthitic alkali-feldspar porphyroblasts were obtained from the felsic granulite sample WG336. In a chondrite normalized spider plot (Fig. 6b), the analysed perthitic alkali-feldspar exhibits enrichments in LREE and depletions in HREE as well as a marked positive Eu anomaly. For detailed LA-ICP-MS mineral chemical data see Table D in the supplementary material.

9. PRESSURE – TEMPERATURE ESTIMATION

In order to constrain the prograde evolution from the onset of garnet core growth in felsic and mafic granulites up to UHT granulite facies peak we applied the Zr-in-rutile thermometry to single rutile grains, enclosed in garnet cores and rims displaying zoning profile type I. For evaluating the full PT path, we additionally estimated PT conditions of the metamorphic peak mineral assemblage and retrograde mineral assemblage by using an approach that consisted of robust net-transfer reactions, feldspar solvus thermometry and Zr-in-rutile thermometry of matrix grains, combined with phase equilibrium modelling (pseudosections). Estimates of these peak and retrograde PT conditions are consistent with results from literature (Carswell and O'Brien, 1993; Kotková and Harley, 1999; Cooke, 2000; Cooke et al., 2000; Cooke and O'Brien, 2001; Štípská and Powell, 2005; Tajčmanová, et al., 2006; Kotková and Harley, 2010).

9.1 Zr-in-rutile thermometry on rutile inclusions within garnets

Both, garnet cores and rims commonly enclose grains of quartz, zircon and anhedral rounded rutile of up to 300 µm in size (Fig. 4a). Based on this observation we conclude that the Zr-content in rutile inclusions is buffered with respect to SiO_2 and ZrO_2 activities by the coexisting quartz and zircon. The rutile inclusions in the high-grossular garnet cores formed during the early prograde metamorphic evolution, whereas those in low-grossular garnet rims are considered to have

recrystallized during the high pressure - ultrahigh temperature granulite facies peak. Corresponding X_{Grs} values of the garnet host mineral were calculated as mean values from three separate analyses 5–10 µm around the rutile inclusion to ensure sufficient spatial resolution. For a detailed summary of rutile analyses, including measured Zr-contents, calculated temperatures following the calibrations of Zack et al. (2004), Ferry and Watson (2007) and Tomkins et al (2007) and corresponding X_{Grs} values see Table F in the supplementary material. Presented temperature estimates in the text are related to the pressure independent calibration of Zack et al. (2004) and the pressure dependent calibration of Tomkins et al. (2007) for an assumed pressure of 1.6 GPa. In the following these two calibrations are referenced as (Z04) and (T07), respectively.

Rutile inclusions in garnet cores of felsic granulites ($0.285 < X_{Grs} > 0.313$) have rather low Zr-contents, ranging from 444 to 814 ppm. Zr-in-rutile thermometry applied to these rutile grains yields an average temperature of ~810 °C (Z04, Fig. 7a) and ~740 °C (T07, Fig. 7b) for this early stage of garnet growth. Rutile grains enclosed within garnet rims of these felsic granulites, which have considerably lower X_{Grs} ($0.030 < X_{Grs} > 0.143$), yield significantly higher Zr-contents, in the range of 1651 to 5774 ppm. The average temperature estimate obtained from these high Zr-rutile grains is ~1030 °C (Z04) and ~930 °C (T07). This higher temperature is in accordance with the PT conditions of c. 1000 °C at 1.6 GPa reported from the literature.

Rutile inclusions within garnet cores and rims from mafic granulites show a similar correlation between calculated temperature and corresponding position in garnet. Rutile grains enclosed in high-grossular garnet cores ($0.354 < X_{Grs} > 0.370$) have low Zr-concentrations (385–1184 ppm) resulting in an average temperature estimate of ~ 820 °C (Z04, Fig. 7c) and ~750 °C (T07, Fig. 7d). In contrast, rutile grains in low-grossular garnet rims ($0.081 < X_{Grs} > 0.166$) have higher Zr contents ranging from 1851 to 5774 ppm yielding significantly higher average temperature estimates of ~1025 °C (Z04) and ~920 °C (T07).

9.2 Peak mineral assemblage

452

453 **9.2.1 Conventional geothermobarometry**

454 To obtain robust estimates for pressures and temperatures of the granulite facies peak
455 mineral assemblages the GASP barometer and the one and two feldspar thermometry are applicable.
456 The GASP reaction was evaluated using the TWEEQU software of Berman (1991, version
457 winTWQ 2.3, updated 1996) with the internally consistent thermodynamic data set of Berman
458 (1988, 1990), as well as with the calibration from Koziol (1989). For the one and two feldspar
459 thermometry, originally established by Fuhrman and Lindsley (1988), we used the ternary feldspar-
460 mixing model after Benisek et al. (2010). Additionally, we applied the trace element Zr-in-rutile
461 thermometer to matrix rutile by using the empirically calibration of Zack et al. (2004) as well as the
462 experimentally calibration of Ferry and Watson (2007) and Tomkins et al. (2007).
463 Carswell and O'Brein (1993), Cooke et al. (2000), Cooke (2000) and Kotková and Harley (2010)
464 pointed out that the application of geothermobarometers to granulites are problematic as the stable
465 mineral assemblage at the peak conditions change their compositions due to diffusional
466 modifications, re-equilibration and/or re-crystallization. In the case of our granulite samples this
467 uncertainty addresses the garnet composition coexisting with a ternary feldspar composition.
468 This ternary feldspar is now represented by perthitic alkali-feldspar which must be re-
469 integrated before being used for estimating peak temperature by the feldspar solvus thermometry.
470 Although this approach is well established, the intensive mylonitisation of our granulite samples
471 leading to a pervasive recrystallization of the feldspar bedevilled our attempt to obtain the original
472 ternary feldspar composition. Consequently, we restricted our geothermobarometric applications by
473 only selecting the very coarsest grained, undeformed perthitic alkali-feldspar porphyroblasts from
474 felsic granulites that display regular exsolution lamellae right up to their grain boundaries. It should
475 be noted that any calculated temperatures for hypothetical coexisting feldspar pairs will give only a
476 minimum temperature, since, at peak granulite facies conditions obviously only one hypersolvus
477 ternary feldspar existed. In this study we have applied the feldspar thermometry method after Kroll

et al. (1993) and feldspar activity models of Benisek et al. (2010) at an assumed pressure of 1.60 GPa. Further we assumed that the hypothetical recovered compositions of the feldspar pairs lie on the same solvus in the ternary feldspar diagram. The one-feldspar thermometric approach on non-equilibrated reintegrated perthitic alkali-feldspar ($An_{5–11}$ $Ab_{17–26}$ $Or_{78–64}$) and the two-feldspar thermometry applied to the same feldspar composition and secondary matrix plagioclase ($An_{17–24}$ $Ab_{80–75}$), provides approximately similar temperature conditions, ranging from 960 up to 1090 °C. We note, however, the occurrence of rare feldspar pairs that gave higher temperature estimates of up to 1150 °C. A comparison of the results of the one- and two-feldspar thermometry is shown on a ternary plot An-Ab-Or in Figure 8.

The preserved garnet zoning in felsic granulites aggravates a clear identification of the actual granulite facies peak garnet composition. As discussed in previous sections garnet rim zones of zoning profile I in very light-coloured, biotite and sillimanite poor felsic granulites (Fig. 3a), display a strong decrease in grossular component at the rim. The decreasing grossular content is matched with an increase in X_{Mg} and is therefore interpreted to reflect prograde garnet growth during temperature increase. Thus, utilizing the composition of garnet rim and the reintegrated perthitic alkali-feldspar composition, the GASP barometer yields peak pressures ranging between ~ 1.45 and ~ 1.70 GPa, at a temperature of 1000 °C. For representative mineral analyses see Table 1 and 3. The combined results of the GASP barometry and the feldspar thermometry indicate PT conditions of 1.60 ± 0.10 GPa and 1000 ± 50°C for the formation of the peak equilibrium mineral assemblage comprising garnet + kyanite + ternary feldspar + quartz.

The granulite facies peak mineral assemblage includes matrix rutile coexisting with quartz and zircon in both felsic and mafic granulites. Consequently, Zr-in-rutile thermometry can be applied in addition to feldspar thermometry (see also Kotková and Harley, 2010). Details of the compositional analyses of all rutile grains, with corresponding Zr-content and calculated temperatures are shown in Table E of the supplementary material. The Zr concentrations of the 51

503 matrix rutile grains analysed are in the range of 1747–5256 ppm, providing temperature estimates
504 of about 940–1090 °C (Z04, Fig. 7e) and 850–990 °C at 1.6 GPa (T07, Fig. 7f).
505
506 **9.2.2 Phase equilibrium modelling**
507 Phase equilibrium modelling calculations were performed over the PT range of 0.6–3.0 GPa
508 and 400–1100 °C, for the ten-component system Mn-NCKFMATSH. We utilised the Gibbs free
509 energy minimization software Theriak/Domino (de Capitani and Brown, 1987; De Capitani, 1994;
510 de Capitani and Petrakakis, 2010, see also:
511 http://titan.minpet.unibas.ch/minpet/theriak/theruser.html), employing the thermodynamic dataset
512 from Holland and Powell (1998) and subsequent updates. The following mixing models were used:
513 Benisek et al. (2010) for feldspar, Coggon and Holland (2002) for white mica, Tajčmanová et al.
514 (2009) for biotite, Holland and Powell (1998) for garnet, Powell and Holland (1999) for
515 orthopyroxene and Holland and Powell (1996) for clinopyroxene. The model utilised for the melt
516 phase was that initially introduced by Holland and Powell (2001) and adapted from White et al.
517 (2001).
518 For meaningful peak PT estimates, a pseudosection was calculated for a weakly deformed,
519 felsic granulite sample with partly preserved granoblastic fabrics, as it represents the dominant
520 high-grade assemblage rock type in investigated granulite bodies. The selected sample is poor in
521 secondary biotite and sillimanite but rich in kyanite, perthitic alkali-feldspar and contains garnet
522 with zoning profile type I (Fig. 3a). It is very siliceous, with a normalized whole rock composition
523 (in weight %) of SiO_2 71.10, TiO_2 0.48, Al_2O_3 14.64, FeO 2.71, MnO 0.039, MgO 0.85, CaO 1.56,
524 Na_2O 2.82, K_2O 4.80, H_2O 1.00. As the sample selected is a very fresh felsic granulite, we assume
525 that it has a very low water content due to metamorphic dehydration reactions. Therefore, for our
526 calculations we have assumed that during the high temperature imprint the water content was 1.00
527 wt.%. In order to evaluate sensitivity, we constructed additional pseudosections using 0.5 % and
528 1.5 % water contents, noting that there were no significant changes in their geometry. As the

529 granulite selected contains only small amounts of garnet and biotite, we concluded that ferric iron
530 was not likely to be an important component in this system. This assumption was supported by a
531 redox-titration analysis, following Yokoyama and Nakamura (2002), which found that the
532 proportion of ferric iron was close to zero. It was recognised that sequestration of chemical
533 components into garnet cores during their growth (Stüwe, 1997) may have altered the effective bulk
534 composition of the rock. Even though we ensured that the selected sample had a low garnet content,
535 we double checked by constructing a pseudosection using a bulk composition calculated by
536 subtracting chemical components incorporated into garnet cores from the whole rock composition.
537 This variation in bulk chemistry had negligible effect to the pseudosection geometry.
538 The resulting pseudosection is shown in Figure 9. The peak metamorphic assemblage
539 observed in thin section comprises garnet + ternary feldspar + kyanite + rutile (+ liquid) + quartz,
540 which is stable at pressures and temperatures higher than 1.40 GPa and 850 °C, respectively. Based
541 on computed isopleths, the grossular content (7 mol.%) at the outer rims of zoning profile type I
542 garnets (Fig. 3a), which are considered to represent equilibrium composition at peak temperatures,
543 and the anorthite content (11 mol.%) of the re-integrated perthitic alkali-feldspar, equilibrium
544 conditions were reached at about 1.70 GPa and 1030 °C (field 1 in Fig. 9a and b). This estimate fits
545 well with PT conditions derived from conventional geothermobarometry (field 2).
546
547 **9.3 Retrograde mineral assemblage**
548
549 **9.3.1 Conventional geothermobarometry**
550 Reasonable temperature estimates of the retrograde assemblage using Fe-Mg exchange
551 thermometry are hampered by continuous diffusional resetting of Fe-Mg ratios during cooling,
552 resulting in temperature underestimation and strong scattering. In contrast, metamorphic conditions
553 calculated from net-transfer reactions are less affected by such retrogressive diffusion processes.
554 Therefore, we applied the amphibole-plagioclase thermometer after Holland and Blundy (1994) to

555 mafic granulites, where petrographic evidence indicated that these minerals had obviously
556 recrystallised during late deformation and are stable phases within the retrograde assemblage
557 together with biotite and ilmenite. These results were combined with calculated pressures by the
558 GASP barometry applied to garnet in biotite-rich domains (Fig. 2d, e) and newly crystallized
559 sillimanite in felsic granulites (TWQ 2.3, Berman, 2007). Undoubtedly garnet in these domains
560 grew under prograde granulite facies conditions. However, they show direct contact with biotite,
561 sillimanite and ilmenite and are thought to have experienced substantial elemental diffusion to have
562 chemically re-equilibrated with the retrograde metamorphic assemblage. Using the composition of
563 these garnet grains and finely grained recrystallized matrix plagioclase, combined with sillimanite,
564 the GASP barometer provides pressure estimates in a narrow range of 0.80–0.85 GPa (assuming a
565 temperature of 760 °C). For detailed mineral chemical analyses used for the calculation see Table 1
566 and 4.
567 The amphibole-plagioclase thermometry applied to mafic granulites, utilizing homogeneous
568 compositions of amphibole and fine-grained recrystallized plagioclase (Table 2 and 4), gives
569 temperature estimates in the narrow range of 740–765 °C (assuming a pressure of 0.80 GPa).
570 Results from felsic and mafic granulites clearly indicate a recrystallization event at about
571 0.85 ±0.1 GPa and 760 ± 50°C. This metamorphic overprint was accompanied by deformation and
572 mylonitization (Figs. 2d,e, i).
573
574 **9.3.2 Phase equilibrium modelling**
575 Additional constraints on the PT conditions of the retrograde mineral assemblage were
576 obtained by constructing a PT pseudosection in the range of 700–850 °C and 0.6–1.1 GPa for the
577 ten-component system Mn-NCKFMATSH (Fig. 10) for a biotite rich domain of a felsic granulite
578 (Fig. 2c), which contains besides biotite the retrograde minerals sillimanite and ilmenite. The
579 normalized whole rock composition (in weight %) is SiO_2 76.75, TiO_2 0.12, Al_2O_3 12.46, FeO 1.49,
580 MnO 0.028, MgO 0.17, CaO 0.40, Na_2O 2.81, K_2O 4.77, H_2O 1.00. As for previous samples

discussed above, a check on the validity of this pseudosection was performed by calculating an alternative pseudosection using an alternative bulk rock composition by subtracting garnet cores from the whole rock XRF analysis. Again, there are no significant differences between the geometries of the two pseudosections generated.

The computed pseudosection (Fig. 10) shows that the retrograde assemblage sillimanite, biotite, plagioclase and ilmenite can only be stable in the presence of both garnet and melt at maximum PT conditions of 770 °C and 0.90 GPa. In this respect, the compositional garnet isopleths of grossular (4 mol.%) in garnet grains from biotite and sillimanite rich domains, suggest that equilibrium for this particular retrograde mineral assemblage was obtained at conditions of approximately 770 °C and 0.8 GPa (field 1 in Fig. 10a and b). These estimates are in good agreement with estimated PT conditions using conventional geothermobarometry (field 2).

10. FE-MG DIFFUSION CHRONOMETRY MODELLING

Diffusion chronometry has been shown to be a powerful tool to extract timescales of cooling and exhumation processes in metamorphic rocks (Müller et al. 2010). We developed a 1-D numerical model to simulate multicomponent diffusion in garnet (Loomis, 1978) to determine the timescales of retrograde re-equilibration processes. Three compositional profiles have been chosen (WG1, WG94, and WG336), that have been identified to be close to central sections and represent type 1 and type 2 profiles. Diffusive element transport in garnet depends on composition, temperature and pressure. Following mineralogical arguments provided by Borinski et al (2012), we limit our model to PT dependent Fe-Mg inter-diffusion and ignore the role of the grossular component. Diffusion coefficients are updated for each timestep and calculated for each node following the data of Borinski et al (2012) and the activation volume of Chakraborty and Ganguly (1992). Müller et al. (2015) has presented convincing evidence that garnet compositions are effectively homogenised independent of the cooling rate above 1000°C. Thus, we model a linear

607 cooling path from 1000 to 750 °C accompanying linear decompression from 1.6 to 0.8 GPa. The
608 initial concentration profile is assumed to have a homogeneous core with an overgrowth rim that is
609 equally homogeneous in composition (dashed lines in Figure 11) assuming fast overgrowth of an
610 existing garnet core of homogeneous composition. Although, this is a substantial simplification, the
611 combination of observed compositional zoning patterns and Zr-in-rutile thermometry data justify
612 the choice of a simple kink-step profile as starting condition. For each individual garnet, the core
613 and boundary compositions have been adjusted to the measured values for each garnet simulation
614 (Fig. 11). The modelled profiles were chosen as being closest to a central section. Inspection of
615 Figure 11, however, reveals that measured profiles are not perfectly symmetric. Nevertheless,
616 modelled profiles still match the data satisfactorily. It is important to bear in mind that any section
617 that is off the central cut will produce a geometrical artefact that will increase the "virtual" diffusion
618 profile and thus result in longer timescales. Hence, the extracted timescales need to be regarded as
619 maximum timescales. The rim thickness was determined to be half of the observed distance
620 between the flat core composition and the garnet interface. We note, that this ignores possible
621 retrograde garnet resorption and thus the profile might have been shortened to some extent.
622 Similarly, modelled timescales of diffusive re-equilibration must be regarded as maximum
623 estimates. Model simulations have been fitted to measured Fe and Mg concentration profiles by
624 varying the run duration. Modelling results of all three garnet profiles representing central sections
625 (including type 1 and type 2) yield timescales for the exhumation and cooling history of 5–6 Ma
626 (Fig. 11). This translates into exhumation rates of 5.3–6.6 mm y^{-1}, and cooling rates of 40–50 °C
627 Ma^{-1}, respectively.
628
629 **11. DISCUSSION**
630
631 **11.1. A key issue: the prograde evolution of the Moldanubian granulites**

There is wide agreement today that the Moldanubian granulites are high pressure - ultra high temperature rocks which experienced conditions of ca. 1000 °C and 1.6–1.8 GPa during the Variscan orogeny. There is also consensus that the rocks then underwent a strong recrystallization during their rapid exhumation to intermediate granulite facies conditions and their subsequent cooling to amphibolite facies conditions (e.g. Vrána, 1992; Kotková and Harley, 1999, 2010; Carswell and O'Brien, 1993; Cooke, 2000; Cooke et al. 2000; Kotkova, 2007; Tajčmanová et al., 2009; Jedlička et al., 2015). However, many uncertainties exist with reference to the prograde PT evolution of the Moldanubian granulites.

For some granulite bodies in the Czech Republic (Kutná Hora and Blanský les), Faryad et al. (2010) showed an incipient phase of eclogite facies metamorphism preceding the granulite facies stage (see also Perraki and Faryad, 2014 and Jedlička et al., 2015). On the other hand, based on an occasionally preserved prograde zoning in garnet and prograde corona reaction textures, Carswell and O'Brien (1993) and Cooke et al. (2000) proposed a prograde PT evolution for the Lower Austrian granulite bodies under amphibolite-facies to granulite facies conditions. These authors excluded that the Lower Austrian granulites did ever experience a typical plagioclase-free eclogite facies imprint, arguing that any eclogite facies assemblages in metabasic rocks intercalated with granulites are completely missing. Only few mantle-derived garnet bearing peridotite lenses tectonically emplaced within the granulite bodies show signs of UHP metamorphism (Carswell and O'Brien, 1993). Available data from the literature is summarized in Figure 12.

The question whether or not the Moldanubian granulites (and which of them) have experienced an eclogite facies precursor stage, is important and absolutely crucial for the tectonic interpretation of this part of the Variscan orogen (see e.g. Schulmann et al. 2009, Finger et al. 2007, Faryad 2009, Faryad et al. 2010). Based on our new petrological observations we discuss this issue below.

11.2. Significance of mineral inclusions in garnet

Preserved primary mineral inclusions in garnet provide the chance to constrain the pre-UHT metamorphic evolution of the granulites. We could not find any eclogite facies mineral relics in the garnets, despite of a careful search. The most abundant primary inclusions in the garnets are: crystallized melt inclusions, Ti-rich biotite, rutile, and composite kaolinite-K-feldspar-quartz inclusions replacing primary muscovite.

Trapped melt inclusions: garnet cores in both felsic and mafic granulites commonly bear small composite inclusions of quartz + K-feldspar + biotite + rutile ± plagioclase ± ilmenite ± apatite (Fig. 4g–i), which can be interpreted as trapped melt. Their high abundance implies a rapid growth rate of the garnet cores, most probably in the course of peritectic garnet producing reactions. Such possible melt and garnet producing reactions are listed below. Reaction (1) is driven by increasing pressure whilst reactions (2), (3), (4), and (5) are overstepped with increasing temperature (Vielzeuf and Holloway, 1988; Patiño Douce, 2005).

bt + als + qz = phe + grt + melt (1)

bt + phe + qz = grt + kfs + melt (2)

phe + qz = grt + kfs + als + melt (3)

bt + als + qz = grt + kfs + melt (4)

phe + cpx + qz = grt + kfs + melt (5)

Biotite: Inclusions of unaltered biotite within the high-grossular garnet cores of felsic granulites (Fig. 4b) have significantly elevated Ti-contents compared to biotites in the matrix. These inclusions are completely surrounded by crack-free hosting garnet and thus belong to the stable mineral assemblage at this stage. Similar biotite inclusions in garnet cores were reported in felsic granulites by Carswell and O'Brien (1993). The solubility of Ti in biotite is mainly a function of temperature, pressure and chemical composition of a biotite grain (Henry et al., 2005 and references therein). Experimental work by Robert (1976) demonstrated that the Ti solubility in biotite is

684 relatively low at 0.1 GPa and 600 °C (0.07 Ti apfu). It increases to 0.20 Ti apfu at 800 °C and to
685 0.70 Ti apfu at 1000 °C. Thus, we conclude that the Ti-rich biotite inclusions in the garnets (with
686 0.333 Ti apfu) were in equilibrium with garnet cores at a temperature of about 800–850 °C.

687 **Composite kaolinite-K-feldspar-quartz inclusions:** The presence of polyphase inclusions
688 of kaolinite (interpreted as hydrated kyanite) + K-feldspar + quartz within garnet cores (Fig. 4f)
689 indicates initial garnet growth in the presence of white mica, which probably subsequently
690 decomposed by the melt producing reaction: muscovite + quartz = K-feldspar + kyanite + melt. In
691 rare cases we have found relics of white mica in the same core regions of garnets.

692 **Rutile inclusions and Zr-in-rutile thermometry:** Rutile inclusions in high-grossular garnet
693 cores show significantly lower Zr-contents compared to those in the low-grossular garnet rims. As
694 rutile grains enclosed in garnet should be largely shielded by diffusive re-equilibration during
695 cooling (Zack et al., 2004) the compositional variability of rutile inclusions from core to rim can be
696 used to determine the temperature evolution during the growth of the garnets and importantly, allow
697 us to define the formation temperature of the early garnet and the subsequent granulite facies peak
698 garnet growth. However, the Zr-in-rutile temperature estimates vary depending on the used
699 calibration. In Figure 7, the empirical calibration of Zack et al. (2004) results in temperatures which
700 are ~80–100 °C higher compared to results from the experimentally calibrated equation of Tomkins
701 et al. (2007) at a pressure of 1.6 GPa. Although the calibration of Zack et al. (2004) does not
702 include a pressure dependent term we use this version of the Zr-in-rutile thermometer due to its
703 consistent results with feldspar solvus thermometry and pseudosection modelling.

704 The Zr-contents of rutile enclosed in the garnet cores from both the felsic and mafic
705 granulites indicate that the majority of garnet cores grew at ~810–820 °C (Fig. 7a). Slightly lower
706 temperatures of 700–800 °C were reported for incipient garnet growth in garnet-clinopyroxene
707 bearing granulites from the St. Leonhard granulite body (Cooke et al., 2000). These temperatures
708 were obtained from the Fe-Mg exchange garnet-clinopyroxene thermometer. As correctly indicated
709 by the authors, these clinopyroxene is only in equilibrium with the HP granulite facies mineral

assemblage and therefore temperature estimates for the early garnet core growth are uncertain. Comparable temperatures (~830 °C) were recently reported from Zr-in-rutile thermometry of rutile inclusions in high-grossular garnets from the Blanský les granulites (Usuki et al. 2017). Considering our results as well as from literature, the garnet cores in the granulites started to nucleate at unusual high T conditions, considerably above the hypothetical equilibrium grt-in reaction as expected for a typical prograde metamorphic evolution of metagranitoids (see Spear, 2017).

The higher Zr content in rutile enclosed in garnet rims of both felsic and mafic granulites give a temperature estimate of ~1030 °C. This result is in good agreement with temperatures of matrix rutile and feldspar solvus thermometry obtained by this study and previous studies (e.g. Kotková and Harley, 2010) and is proof of the garnet rim growth during the HP-UHT granulite facies stage.

11.3. Garnet growth history revealed by trace element zoning

Both, major and trace elements show a nearly flat zoning profile over a broad core region but change sharply at the rim. The changes in trace elements at the rim occurs over a shorter distance compared to major elements, reflecting their lower susceptibility to diffusion within the garnet structure and makes them more likely to record earlier evolutionary stages (e.g. Spear and Kohn, 1996). The homogeneous and flat zoning of trace elements (P, Ti, Zr, Y, V, Cr, Ga and REE) in the broad garnet core region implies that this part of the garnet formed during a single garnet forming reaction at a narrow PT range. Considering the relatively high Ti-content of about 900 ppm in the garnet core, we interpret that a Ti-rich reactant mineral was involved in the garnet forming reaction. Since high-Ti biotite is a common inclusion it is likely that the garnet cores grew at the expense of biotite. Based on the Zr-in-rutile temperature estimate of 810–820 °C for the garnet core growth, reaction (1) bt + als + qz = phe + grt + melt is considered to be responsible for garnet core growth during pressure increase.

735 The sharp decrease of Ti within the garnet rim region as well as sharp changes in other trace
736 elements suggest that the UHT rims formed by different garnet producing reactions. We speculate
737 that the UHT garnet rims formed by incongruent melting reactions involving phengitic white mica
738 (±clinopyroxene), for instance by reactions (3) or (5). The kyanite consuming reaction (4) is less
739 likely since kyanite is part of the granulite facies peak mineral assemblage. Also, reaction (2), which
740 requires biotite, was probably not involved, as indicated by the low Ti-content in the garnet rims.
741 The significant drop of Zr within the garnet rims may be explained by enhanced crystallisation of
742 rutile which incorporates high amounts of Zr at UHT conditions. The increase in V, Cr, and Ga at
743 the outermost garnet rim is interpreted as the result of white mica decomposition en route to peak
744 granulite facies conditions. The elevated contents of P, Y and LREE in the garnet core and the
745 pronounced drop of these elements at the rim indicate that garnet core grew prior to significant
746 ternary feldspar and apatite crystallization. Similar observations has been reported from leucocratic
747 granulites in the Blanský les Massif (Kotková and Harley, 2010).
748
749 **11.4. Possible geological scenario**
750 The new data presented and discussed above strongly suggest that the prograde PT evolution
751 of the granulite bodies in the southeastern Moldanubian Zone involved two separate stages: (1) the
752 UHT stage of ~ 1000 °C and 1.6 GPa, which has been documented in a number of earlier studies as
753 well (see Kotková, 2007 for review), and (2) a preceding lower-T metamorphic stage which is
754 represented by the garnet cores and their inclusions. This stage occurred at temperatures of ~810–
755 820 °C. Unfortunately, we do not have precise constraints on the pressure conditions of this stage.
756 Rutile inclusions in the garnet cores define a lower pressure limit of ~1.2 GPa (Fig. 13). If the
757 garnet cores formed by overstepping of the biotite consuming peritectic reaction (1), what we
758 consider most likely, then the pressure should have been at around 1.6 GPa. Experimental data by
759 Hermann (2002) showed that Ti-rich biotite can be stable up to ~2.5 GPa at ~810–820 °C, setting
760 the upper pressure limit for the early garnet core formation. Assuming a geothermal gradient of ~10

°C/km, which is observed in subduction settings with fast plate motion, pressures of 2.0–2.5 GPa could be reached at a temperature of ~810–820 °C. At a higher geothermal gradient of ~20 °C/km, the peritectic reaction (1) is overstepped at significantly lower pressure (~1.5–2.0 GPa).

Depending on the geometry of the prograde path (Fig. 13), the subsequent granulite facies event was either (a) caused by isobaric heating (likely in case of a geothermal gradient of 20 °C/km), or (b) by decompression and contemporaneous heating or (c) isothermal decompression followed by heating (likely in case of a thermal gradient of 10 °C/km). The ultimate cause for the UHT metamorphism was most likely the introduction of mantle heat, either provided by slab breakoff (Finger et al., 2007), mantle delamination (Massone, 2006) or slab roll back (Sizova et al., 2018). As a result, the superheated, partially molten crustal material becomes highly mobile and "flows" upward into a mid-crustal position where it re-equilibrates (Schulmann et al. 2009).

11.5. Exhumation and cooling history of the Lower Austrian granulites

Previous studies concluded that the exhumation and cooling rates of the Moldanubian granulites were in a range of. 2.9–3.5 mm year^{-1} and 7–20 °C myr^{-1}, respectively (Svojtka et al., 2002; Tajčmanová et al., 2006). These numbers are based on either an extrusion model or a combination of petrographic observations and zircon dating in multiple rock units. In this study we use a combination of methods (geothermobarometry, pseudosections and diffusion chronometry) on individual rock specimens. In all cases, we determined a minimum uplift of 5.3–6.6 mm year^{-1} and cooling rates of 40–50 °C myr^{-1}. Thus, our results indicate a much faster exhumation compared to previous results for Moldanubian granulites. We note, however, that these estimates are still about an order of magnitude lower than those simulated for the uplift of mantle xenoliths further north in the Granulite Massif (Müller et al., 2015). Hence, we interpret our rates which are based on a holistic approach to be realistic and provide estimates of the steep exhumation and cooling history from peak HP granulite facies conditions to lower granulite/amphibolite facies conditions.

786 The proposed PT evolution for granulites from this study area differs from the PT path of
787 granulites from the northern and central part of the Moldanubian Zone (Blanský les and Kutná Hora
788 granulite). In the latter, an eclogite facies evolution at about 700 °C at 3.2–4.0 GPa was reported
789 based mainly on ultra-high pressure phases included in garnet (Faryad et al., 2010; Perraki and
790 Faryad, 2014). Our study does not provide any evidence for such an UHP imprint for the large
791 granulite bodies in the southeastern part of the Moldanubian Zone. Nevertheless, we do not
792 necessarily rule out a PT path up to coesite or diamond stability (Fig. 13), since relics of this UHP
793 evolution are likely to be of limited extent and extremely rare in these granulites.
794
795 **12. Conclusions**
796
797 1. Rutile inclusions in garnet and application of the Zr-in-rutile thermometry provides a tool to
798 improve our understanding of the prograde metamorphic evolution of granulites from the
799 Moldanubian Zone. Garnet cores with high grossular content formed at a temperature of
800 ~810–820 °C contemporaneous with extensive melting recorded in abundant polycrystalline
801 melt inclusions throughout these cores. The presence of high-Ti biotite inclusions within the
802 garnet cores constrains confining pressures between 1.6 and 2.5 GPa.
803 2. Rutile inclusions in low-grossular rims of the same garnets record UHT conditions at
804 ~1030 °C. This temperature is within errors to T estimates of 1000 ± 50 °C based on
805 conventional geothermobarometry and pseudosection phase diagrams. Pressure was estimated
806 with 1.60 ± 0.10 GPa for the garnet rim growth.
807 3. High-grossular garnet cores from felsic granulites do not show significant compositional
808 changes in trace elements indicating a single reaction (peritectic biotite breakdown reaction)
809 for the garnet core crystallization. In contrast, the sharp changes in trace element contents
810 within the rim of garnets implies different garnet forming reaction(s).The low-grossular
811 garnet rim was most likely formed by incongruent phengitic white mica consuming and melt

producing reactions. Also white mica is not observed as a matrix mineral phase, inclusions in garnet confirm the presence of white mica during the prograde PT path.

4. The pronounced zoning of major elements at the garnet rim despite UHT conditions points to an extremely short lived metamorphic episode. Otherwise diffusion would have homogenised the garnet right through to its core. Therefore, the garnet rim must have formed rapidly, probably due to a certain overstepping of the garnet rim forming reactions.
5. Binary Fe-Mg diffusion chronometry on garnet profiles indicates that the Moldanubian granulites in the southeastern Bohemian Massif underwent rapid exhumation and cooling (~4.4–5.3 mm y^{-1} and ~40–50 °C Myr^{-1}) subsequent to granulite facies peak conditions.

Acknowledgements

S.W. Faryad, H. Fritz and K. Stüwe are thanked for their comments and critical discussions and J.E. Booth for English editing of the manuscript. D. Sorger and E. Sizova are thanked for their support and comments. K. Ettinger assistance at microprobe work is thankfully acknowledged. A. Benisek is thanked for his help with the ternary feldspar thermometry. The paper benefited from constructive and detailed reviews by R. Jedlička and two anonymous reviewers, as well as editorial handling by M. Scambelluri. This research did not receive any specific grant from funding agencies in the public, commercial, or not-for-profit sectors.

References

Arnold, A., Scharbert, H.G., 1973. Rb-Sr Altersbestimmungen an Granuliten der südlichen Böhmischen Masse in Österreich. Schweizerische mineralogische und petrografische Mitteilungen 53, 61–78.

838 Baba, S., 2003. Two stages of sapphirine formation during prograde and retrograde metamorphism
839 in the Palaeoproterozoic Lewisian complex in South Harris, NW Scotland. Journal of Petrology 44,
840 329–354.
841
842 Benisek, A., Dachs, E., Kroll, H., 2010. A ternary feldspar-mixing model based on calorimetric
843 data: development and application. Contributions to Mineralogy and Petrology 160, 327–337.
844
845 Berman, R.G., 1988. Internally-consistent thermodynamic data for minerals in the system Na2O-
846 K2O-CaO-MgO-FeO-Fe2O3-Al2O3-SiO2-TiO2-H2O-CO2. Journal of Petrology 29, 445–522.
847
848 Berman, R.G., 1990. Mixing properties of Ca-Mg-Fe-Mn garnets. American Mineralogist 75, 328–
849 344.
850
851 Berman, R.G., 1991. Thermobarometry using multi-equilibrium calculations: a new technique, with
852 petrological applications. The Canadian Mineralogist 29, 833–855.
853
854 Berman, R.G., 2007. WinTWQ (version 2.3): A software package for performing internally-
855 consistent thermobarometric calculations. Geological Survey of Canada Open File 5462, pp. 1–41.
856
857 Borinski, S.A., Hoppe, U., Chakraborty, S., Ganguly, J., Bhowmik, S.K. (2012). Multicomponent
858 diffusion in garnets I: general theoretical considerations and experimental data for Fe-Mg systems.
859 Contributions to Mineralogy and Petrology, 164, 571–586.
860
861 Brückner, H.K., Medaris, L.G., Bakun-Czubarow, N., 1991. Nd and Sr age and isotope patterns
862 from Variscan eclogites of the eastern Bohemian Massif. Neues Jahrbuch für Mineralogie,
863 Abhandlungen 163, 169–196.

Caporuscio, F.A., Morse, S.A., 1978. Occurrence of sapphirine plus quartz at Peekskill, New York. American Journal of Science 278, 1334–1342.

Carswell, D.A., Jamtveit, B., 1990. Variscan Sm-Nd ages for the high-pressure metamorphism in the Moldanubian Zone of the Bohemian Massif, Lower Austria. Neues Jahrbuch für Mineralogie, Abhandlungen 162, 69–78.

Carswell, D.A., O'Brien, P.J., 1993. Thermobarometry and geotectonic significance of high pressure granulites: examples from the Moldanubian Zone of the Bohemian Massif in Lower Austria. Journal of Petrology 34, 427–459.

Chakraborty, S., Ganguly, J., 1992. Cation diffusion in aluminosilicate garnets: experimental determination in spessartine-almandine diffusion couples, evaluation of effective binary diffusion coefficients, and applications. Contributions to Mineralogy and Petrology 111, 74–86.

Coggon, R., Holland, T.J.B., 2002. Mixing properties of phengitic micas and revised garnet-phengite thermobarometers. Journal of Metamorphic Geology 20, 683–696.

Cooke, R.A., 2000. High-pressure/temperature metamorphism in the St. Leonhard Granulite Massif, Austria: evidence from intermediate pyroxene-bearing granulites. International Journal of Earth Sciences 89, 631–651.

Cooke, R.A., O'Brien, P.J., Carswell, D.A., 2000. Garnet zoning and the identification of equilibrium mineral compositions in high-pressure-temperature granulite from the Moldanubian Zone, Austria. Journal of metamorphic Geology 18, 551–569.

Cooke, R.A., O'Brien, P.J., 2001. Resolving the relationship between high P–T rocks and gneisses in collisional terranes: an example from the Gföhl gneiss–granulite association in the Moldanubian Zone, Austria. Lithos 58, 33–54.

de Capitani, C.D., Brown, T.H., 1987. The computation of chemical equilibrium in complex systems containing non-ideal solutions. Geochimica et Cosmochimica Acta 51, 2639–2652.

de Capitani, C.D., 1994. Gleichgewichts-phasendiagramme: theorie und software. Berichte der Deutschen Mineralogischen Gesellschaft 6, 48.

de Capitani, C.D., Petrakakis, K., 2010. The computation of equilibrium assemblage diagrams with Theriak/Domino software. American Mineralogist 95, 1006–1016.

Droop, G.T.R., Bucher-Nurminen, K., 1984. Reaction textures and metamorphic evolution of sapphirine-bearing granulites from the Gruf Complex, Italian Central Alps. Journal of Petrology 25, 766–803.

Faryad, S.W., 2009. The Kutná Hora Complex (Moldanubian zone, Bohemian Massif): A composite of crustal and mantle rocks subducted to HP/UHP conditions. Lithos 109, 193–208.

Faryad, S.W., Dolejš, D., Machek, M., 2009. Garnet exsolution in pyroxene from clinopyroxenites in the Moldanubian zone: constraining the early pre- convergence history of ultramafic rocks in the Variscan orogen. Journal of Metamorphic Geology 27, 655–671.

915 Faryad, S.W., Nahodilová, R., Dolejš, D., 2010. Incipient eclogite facies metamorphism in the
916 Moldanubian granulites revealed by mineral inclusions in garnet. Lithos 114, 54–69.
917
918 Faryad, S.W., Kachlík, V., Sláma, J, Hoinkes, G., 2015. Implication of corona formation in a
919 metatroctolite to the granulite facies overprint of HP–UHP rocks in the Moldanubian Zone
920 (Bohemian Massif). Journal of Metamorphic Geology 33, 295–310.
921
922 Ferry, J.M., Watson, E.B., 2007. New thermodynamic models and revised calibrations for the Ti-in-
923 zircon and Zr-in-rutile thermometers. Contributions to Mineralogy and Petrology 154, 429–437.
924
925 Fiala, J., Matejovska, O., Vankova, A., 1987. Moldanubian granulites: source material and
926 petrogenetic considerations. Neues Jahrbuch für Mineralogie-Abhandlungen 157, 133-65.
927
928 Finger, F., Gerdes, A., Janoušek, V., René, M., Riegler, G., 2007. Resolving the Variscan evolution
929 of the Moldanubian sector of the Bohemian Massif: the significance of the Bavarian and the
930 Moravo-Moldanubian tectonometamorphic phases. Journal of Geosciences 52, 9–28.
931
932 Frank, W., Hammer, S., Popp, F., Scharbert, S., Thöni, M., 1990. Isotopengeologische
933 Neuergebnisse zur Entwicklungsgeschichte der Böhmischen Masse. Österreichische Beiträge zu
934 Meteorologie und Geophysik 3, 185–228.
935
936 Franke, W., 2000. The mid-European segment of the Variscides: tectonostratigraphic
937 units, terrane boundaries and plate evolution. In: Franke, W., Haak, V., Oncken, O.,
938 Tanner, D. (Eds.), Orogenic Processes: Quantification and Modelling in the Variscan
939 Belt. Geol. Soc. London, Spec. Publ., London, 179, pp. 35-61.
940

941 Friedl, G., Fritz, F., Paquette, J-L., on Quadt, A., McNaughton, N.J., Fletcher, I.R., 2004. Pre-
942 Variscan geological events in the Austrian part of the Bohemian Massif deduced from U-Pb zircon
943 ages. International Jouranl of Earth Sciences 93, 802–823.
944
945 Friedl, G., Cooke, R.A., Finger, F., McNaughton, N.J., Fletcher, I.R., 2011. Timing of Variscan HP-
946 HT metamorphism in the Moldanubian Zone of the Bohemian Massif: U-Pb SHRIMP dating on
947 multiply zoned zircons from a granulite from the Dunkelsteiner Wald Massif, Lower Austria.
948 Mineralogy and Petrology 102, 63–75.
949
950 Fuchs, G., Matura, A., 1968. Die Böhmische Masse in Österreich, in: Geologische Bundesanstalt
951 (Eds.), Der Geologische Aufbau Österreichs. Springer, Vienna, pp. 121–143.
952
953 Fuhrman, M.L., Lindsley, D.H., 1988. Ternary-feldspar modeling and thermometry. American
954 Mineralogist 73, 201–215.
955
956 Harley, S.L., 1998. On the occurrence and characterization of ultrahigh-temperature crustal
957 metamorphism. In: Treloar, P.J., O'Brien, P.J. (Eds.), What Drives Metamorphism and Metamorphic
958 Reactions? Special Publications 138, Geological Society, London, 81–107.
959
960 Hauzenberger, C.A., Robl, J., Stüwe, K., 2005. Garnet zoning in high pressure granulite-facies
961 metapelites, Mozambiquebelt, SE-Kenya: constraints on the cooling history. European Journal of
962 Mineralogy 17, 43–55.
963
964 Henry, D.J., Guidotti, C.V, Thomason, J.A., 2005. The Ti-saturation surface for low-to-medium
965 pressure metapelitic biotites: Implications for geothermometry and Ti-substitution mechanisms.
966 American Mineraologies 90, 316–328.

967

968 Hermann, J., 2002. Experimental constraints on phase relations in subducted continental crust.
969 Contribution to Mineralogy and Petrology 143, 219–235.
970

971 Holland, T.J.B., Blundy, J., 1994. Non-ideal interactions in calcic amphiboles and their bearing on
972 amphibole-plagioclase thermometry. Contributions to Mineralogy and Petrology 116, 433–447.
973

974 Holland, T.J.B., Powell, R., 1996. Thermodynamics of order-disorder in minerals: II. Symmetric
975 formalism applied to solid solutions. American Mineralogist 81, 1425–1437.
976

977 Holland, T.J.B., Powell, R., 1998. An internally consistent thermodynamic data set for phases of
978 petrological interest. Journal of metamorphic Geology 16, 309–343.
979

980 Holland, T.J.B., Powell, R., 2001. Calculation of phase relations involving haplogranitic melts using
981 an internally consistent thermodynamic dataset. Journal of Petrology 42, 673–683.
982

983 Janoušek, V., Finger, F., Roberts, M.P., Frýda, J., Pin, C., Dolejš, D., 2004. Deciphering
984 petrogenesis of deeply buried granites: whole-rock geochemical constraints on the origin of largely
985 undepleted felsic granulites from the Moldanubian Zone of the Bohemian Massif. Transactions of
986 the Royal Society of Edinburgh: Earth Sciences 95, 141–159.
987

988 Jedlička, R., Faryad, S.W., Hauzenberger, C.A., 2015. Prograde metamorphic history of UHP
989 granulites from the Moldanubian Zone (Bohemian Massif) revealed by major element and Y+ REE
990 zoning in garnets. Journal of Petrology 56, 2069–2088.
991

992 Jochum, K.P., Weis, U., Stoll, B., Kuzmin, D., Yang, Q., Raczek, I., Jacob, D. E., Stracke, A.,
993 Birbaum, K., Frick, D. A., Günther, D., Enzweiler, J., 2011. Determination of reference values for
994 NIST SRM 610–617 glasses following ISO guidelines. Geostandards and Geoanalytical Research
995 35, 397–429.
996
997 Kelly, N.M., Harley, S.L., 2004. Orthopyroxene–corundum in Mg–Al-rich granulites from the
998 Oygarden Islands, East Antarctica. Journal of Petrology 45, 1481–1512.
999
1000 Kotková, J., 2007. High-pressure granulites of the Bohemian Massif: recent advances and open
1001 questions. Journal of Geosciences 52, 45–71.
1002
1003 Kotková, J., Harley, S.L., 1999. Formation and evolution of high-pressure leucogranulites:
1004 experimental constraints and unresolved issues. Physics and Chemistry of the Earth, Part A: Solid
1005 Earth and Geodesy 24, 299–304.
1006
1007 Kotková, J., Harley, S.L., 2010. Anatexis during High-pressure Crustal Metamorphism: Evidence
1008 from Garnet–Whole-rock REE Relationships and Zircon–Rutile Ti–Zr Thermometry in
1009 Leucogranulites from the Bohemian Massif. Journal of Petrology 51, 1967–2001.
1010
1011 Koziol, A.M., 1989. Recalibration of the garnet-plagioclase Al2SiO5-quartz (GASP) geobarometer
1012 and applications for natural parageneses. EOS Transactions American Geophysical Union 70, 493.
1013
1014 Kroll, H., Evangelakakis, C., Voll, G., 1993. Two-feldspar geothermometry: a review and revision
1015 for slowly cooled rocks. Contributions to Mineralogy and petrology 114, 510–518.
1016

1017 Kröner, A., O'Brien, P.J., Nemchin, A.A., Pidgeon, R.T., 2000. Zircon ages for high pressure
1018 granulites from South Bohemia, Czech Republic, and their connection to Carboniferous high
1019 temperature processes. Contributions to Mineralogy and Petrology 138, 127–42.
1020
1021 Loomis, T.P., Ganguly, J., Elphick, S.C., 1985. Experimental determination of cation diffusivities in
1022 aluminosilicate garnets II. Multicomponent simulation and tracer diffusion coefficients.
1023 Contributions to Mineralogy and Petrology 90, 45–51.
1024
1025 Massone, H.J., 2006. Early metamorphic evolution and exhumation of felsic high-pressure
1026 granulites from the north-western Bohemian Massif. Mineralogy and Petrology 86, 177–202.
1027
1028 Müller, T., Watson, E.B., Harrison, T.M., 2010. Applications of diffusion data to high-temperature
1029 earth systems. Reviews in mineralogy and geochemistry 72, 997–1038.
1030
1031 Müller, T., Massone, H.-J., Willner, A.P., 2015. Timescales of exhumation and cooling inferred by
1032 kinetic modelling: An example using a lamellar garnet pyroxenite from Variscan Granulitgebirge, E
1033 Germany. American Mineralogist 100, 747–759.
1034
1035 Nakamura, N., 1974. Determination of REE, Ba, Fe, Mg, Na and K in carbonaceous and ordinary
1036 chondrites. Geochimica et Cosmochimica Acta 38, 757–775.
1037
1038 O'Brien, P.J., Kröner, A., Jaeckel, P., Hegner, E., Zelazniewicz, A., Kryza, R., 1997. Petrological
1039 and isotopic studies on Palaeozoic high-pressure granulites, Gory Sowie Mts, Polish Sudetes.
1040 Journal of Petrology 38, 433–456.
1041

1042 O'Brien, P.J., Rötzler, J., 2003. High-pressure granulites: formation, recovery of peak conditions
1043 and implications for tectonics. Journal of Metamorphic Geology 2, 3–20.
1044
1045 Osanai, Y., Sajeev, K., Owada, M., Kehelpannala, K.V.W., Prame, W.K.B., Nakano, N., Jayatileke,
1046 S., 2006. Metamorphic evolution of high-pressure and ultrahigh-temperature granulites from the
1047 Highland Complex, Sri Lanka. Journal of Asian Earth Sciences 28, 20–37.
1048
1049 Patiño Douce, A.E., 2005. Vapor-absent melting of tonalite at 15–32 kbar. Journal of Petrology 46,
1050 275–290.
1051
1052 Perraki, M., Faryad, S.W., 2014. First finding of microdiamond, coesite and other UHP phases in
1053 felsic granulites in the Moldanubian Zone: Implications for deep subduction and a revised
1054 geodynamic model for Variscan Orogeny in the Bohemian Massif. Lithos 202, 157–166.
1055
1056 Petrakakis, K., 1997. Evolution of Moldanubian rocks in Austria: review and synthesis. Journal of
1057 Metamorphic Geology 15, 203–222.
1058
1059 Powell, R., Holland, T.J.B., 1999. Relating formulations of the thermodynamics of mineral solid
1060 solutions: activity modeling of pyroxenes, amphiboles, and micas. American Mineralogist 84, 1–14.
1061
1062 Prince, C.I., Košler, J., Vance, D., Günter, D., 2000. Comparison of laser ablation ICP-MS and
1063 isotope dilution REE analyses—implications for Sm–Nd garnet geochronology. Chemical Geology
1064 168, 255–274.
1065

1066 Raase, P., 1998. Feldspar thermometry: A valuable tool for deciphering the thermal history of
1067 granulite-facies rocks, as illustrated with metapelites from Sri Lanka. The Canadian Mineralogist
1068 36, 67–86.
1069
1070 Robert, J.L., 1976. Titanium solubility in synthetic phlogopite solid solutions. Chemical Geology
1071 17, 213–227.
1072
1073 Rötzler, J., Romer, R.L., 2001. P–T–t evolution of ultrahigh-temperature granulites from the Saxon
1074 Granulite Massif, Germany. Part I: petrology. Journal of Petrology 42, 1995–2013.
1075
1076 Sandiford, M., Neale, F., Powell, R., 1987. Metamorphic evolution of aluminous granulites from
1077 Labwor Hills, Uganda. Contributions to Mineralogy and Petrology 95, 217–225.
1078
1079 Scharbert, H.G., Kurat, G., 1974. Distribution of some elements between coexisting ferromagnesian
1080 minerals in Moldanubian granulite facies rocks, Lower Austria, Austria. Tschermaks
1081 Mineralogische und Petrographische Mitteilungen 21, 110–134.
1082
1083 Schnabel, W., Bryda, G., Egger, H., Fuchs, G., Matura, A., Krenmayr, H.G., Mandl, G.W.,
1084 Nowotny, A., Roetzel, R., Scharbert, S., Wessely, G., 2002. Geologische Karte von Niederösterreich
1085 1:200000. Land Niederösterreich und Geologische Bundesanstalt.
1086
1087 Schulmann, K., Konopásek, J., Janoušek, V., Lexa, O., Lardeaux, J.-M., Edel, J.B., Štípská, P.,
1088 Ulrich, S., 2009. An Andean type Palaeozoic convergence in the Bohemian Massif. Comptes
1089 Rendus Geoscience 341, 266–286.
1090

1091 Sizova, E., Gerya, T., Brown, M., Stüwe, K., Hauzenberger, C., Fritz, H., Faryad, S.W., 2018.
1092 Overprinting metamorphic events during continental collision: Insight from geodynamic modelling.
1093 Granulites and Granulites 2018, Ullapool, Scotland.
1094
1095 Spear, F. S., 2017. Garnet growth after overstepping. Chemical Geology 466, 491–499.
1096
1097 Spear, F.S., Kohn, M.J., 1996. Trace element zoning in garnet as a monitor of crustal melting.
1098 Geology 24, 1099–1102.
1099
1100 Štípská, P., Powell, R., 2005. Does ternary feldspar constrain the metamorphic conditions of high-
1101 grade meta-igneous rocks? Evidence from orthopyroxene granulites, Bohemian Massif. Journal of
1102 Metamorphic Geology 23, 627–647.
1103
1104 Stüwe, K., 1997. Effective bulk composition changes due to cooling: a model predicting
1105 complexities in retrograde reaction textures. Contributions to Mineralogy and Petrology 129, 43–
1106 52.
1107
1108 Svojtka, M., Košler, J.,· Venera, Z., 2002. Dating granulite-facies structures and the exhumation of
1109 lower crust in the Moldanubian Zone of the Bohemian Massif. International Journal of Earth
1110 Science 91, 373–385.
1111
1112 Tajčmanová, L., Konopásek, J. Schulmann, K., 2006. Thermal evolution of the orogenic lower crust
1113 during exhumation within a thickened Moldanubian root of the Variscan belt of Central Europe.
1114 Journal of Metamorphic Geology 24, 119–134.
1115

1116 Tajčmanová, L., Connolly, J.A.D., Cesare, B., 2009. A thermodynamic model for titanium and ferric
1117 iron solution in biotite. Journal of metamorphic Geology 27, 153–165.
1118
1119 Tomkins, H.S., Powell, R., Ellis, D.J., 2007. The pressure dependence of the zirconium-in-rutile
1120 thermometer. Journal of Metamorphic Geology 25, 703–713.
1121
1122 Tropper, P., Hauzenberger, C., 2015. How well do pseudosection calculations reproduce simple
1123 experiments using natural rocks: an example from high-P high-T granulites of the Bohemian
1124 Massif. Austrian Journal of Earth Sciences 108, 123–138.
1125
1126 Usuki, T., Iizuka, Y., Hirajima, T., Svojtka, M., Lee, H.Y., Jahn, B.M., 2017. Significance of Zr-in-
1127 Rutile Thermometry for Deducing the Decompression P–T Path of a Garnet–Clinopyroxene
1128 Granulite in the Moldanubian Zone of the Bohemian Massif. Journal of Petrology 58, 1173–1198.
1129
1130 Vielzeuf, D., Holloway, J.R., 1988. Experimental determination of the fluid-absent melting relations
1131 in the pelitic system: Consequences for crustal differentiation. Contribution to Mineralogy and
1132 Petrology 98, 257–276.
1133
1134 Vrána, S., 1992. The Moldanubian Zone in southern Bohemia: polyphase evolution of imbricated
1135 crustal and upper mantle segments. in: Kukal, Z. (Eds.), International Conference on Bohemian
1136 Massif. Czech Geological Survey, Prague, pp. 331–336.
1137
1138 Vrána, S., Štědrá, V., Fišera, M., 2005. Petrology and geochemistry of the Běstvina granulite body
1139 metamorphosed at eclogite facies conditions, Bohemian Massif. Journal of the Czech Geological
1140 Society 50, 81–94.
1141

White, R.W., Powell, R., Holland, T.J.B., 2001. Calculation of partial melting equilibria in the system Na2O–CaO–K2O–FeO–MgO–Al2O3–SiO2–H2O (NCKFMASH). Journal of Metamorphic Geology 19, 139–153.

Whitney, D.L., Evans, B. W., 2010. Abbreviations for names of rock-forming minerals. American Mineralogist 95, 185–187.

Yokoyama, T., Nakamura, E., 2002. Precise determination of ferrous iron in silicate rocks. Geochimica et Cosmochimica Acta 66, 1085–1093.

Zack, T., Moraes, R., Kronz, A., 2004. Temperature dependence of Zr in rutile: empirical calibration of a rutile thermometer. Contributions to Mineralogy and Petrology 148, 471–488.

Figure Captions

Fig. 1. (a) Simplified geological framework of the Bohemian Massif (modified after Franke, 2000). Upper left inset shows the tectonic subdivision of the central European Variscides. Letters indicate granulite bodies in the Moldanubian Zone: DW – Dunkelsteinerwald granulite, PW – Pöchlarn-Wiselburg granulite, SL – St. Leonhard granulite, B – Blumau granulite, J – Jemnice granulite, Mo – Mohelno granulite, SU –Strážek Unit granulite, KH – Kutná Hora granulite, L – Lišov granulite, Bl – Blanský les granulite, P – Prachatice granulite, K – Křištánov granulite. (b) Simplified geological map of the southeastern Bohemian Massif (modified after Schnabel et al., 2002).

Fig. 2. Hand-specimen photographs and corresponding photomicrographs of (a) a felsic granulite containing (b) the HP granulite facies peak mineral assemblage of garnet + kyanite + peritectic alkali-feldspar + rutile + quartz; (c) a felsic granulite with slightly darker bands where (d, e)

retrogressive biotite-flakes interpenetrate sillimanite and ilmenite to form masses oriented parallel to the foliation, mainly defined by quartz ribbons; (f) a fresh mafic granulite with (g) large porphyroblasts of peak garnet and antiperthitic plagioclase and randomly distributed, small secondary orthopyroxene and biotite in a quartzo-feldspathic matrix; (h) a strongly retrograde mafic granulite with (i, j) secondary amphibole, biotite and ilmenite intergrown with small garnet.

Fig. 3. BSE images and major element zoning profiles of representative garnets from felsic (a, b, c, d, e) and mafic (f) granulites. Y-axes indicates mol. % of garnet endmembers; x-axes indicate rim-core-rim distances in millimetres.

Fig. 4. Photomicrographs of representative inclusions. (a) Rounded, anhedral rutile within garnet. (b) Euhedral inclusion of fresh high-Ti biotite in garnet core. (c) Perthitic alkali-feldspar within kyanite reflecting the equilibrium coexistence between ternary feldspar and kyanite at granulite facies peak conditions. (d) Euhedral-shaped diopside dominated clinopyroxene in the medium to low Ca garnet zone of a mafic granulite, note this is a garnet rim section. (e) Relics of white mica, quartz, biotite and rutile form a polyphase inclusion in the Ca-rich garnet core region; (f) Inclusion of kaolinite, K-feldspar and randomly decomposed quartz in garnet core, most probably formed after the muscovite break-down. (g) Numerous small melt inclusions within garnet core and rim areas. Inset shows a zoom-in where the euhedral-shaped melt inclusions are located in a crack-free garnet domain. (h, i) Euhedral-shaped polycrystalline melt inclusion composed of quartz, K-feldspar and biotite.

Fig. 5. Garnet profile type I from felsic granulite WG336, major element compositional maps of Ca, Fe, Mg, (b–d), major element zoning (e), trace element and REE zoning (f–p) and chondrite normalized Rare Earth Element plot (q) for garnet core and garnet rim. Y-axes indicates ppm of trace elements; x-axes indicate rim-core-rim distances in millimetres. Note zoning of selected trace

1194 elements were slightly smoothed. Rim-core-rim boundaries are based on the trace element changes
1195 in (e).
1196
1197 **Fig. 6.** Chondrite normalized Rare Earth Element plot for (a) apatite in garnet core, garnet rim and
1198 rock matrix and (b) perthitic alkali-feldspar.
1199
1200 **Fig. 7.** Plot of calculated Zr-in-rutile temperatures against (a, b) X_{Grs} of garnet host enclosing rutile
1201 in felsic granulites and (c, d) X_{Grs} of garnet host enclosing rutile in mafic granulites. Red squares
1202 and green diamonds indicate measured rutiles in low grossular garnet rim and high grossular garnet
1203 core regions, respectively. (c, d) Zr-contents of matrix rutiles (grey diamonds) in felsic and mafic
1204 granulites vs calculated temperatures. Temperature estimates are after Zack et al. (2004) - Z (04) and
1205 Tomkins et al. (2007) - (T07) for an assumed pressure of 1.6 GPa.
1206
1207 **Fig. 8.** Exemplary feldspar pairs using the one feldspar (open symbols) and two feldspar (full
1208 symbols) thermometry for a given pressure of 1.60 GPa. Temperature isopleths are obtained using
1209 the recent interaction parameters of Benisek et al. (2010) for 1.60 GPa.
1210
1211 **Fig. 9.** PT pseudosection for the granulite facies peak mineral assemblage. (a) Presents fields of
1212 stable mineral assemblages and volume isopleths of garnet. Important phase transitions are indicated
1213 as bold coloured lines. Labels for small PT fields are omitted for avoiding confusion. (b) Presents
1214 isopleths of grossular and anorthite in ternary feldspar.
1215
1216 **Fig. 10.** PT pseudosection for the retrograde mineral assemblage. (a) Presents fields of stable
1217 mineral assemblages and volume isopleths of garnet. Important phase transitions are indicated as
1218 bold coloured lines. Labels for small PT fields are omitted for avoiding confusion. (b) Presents
1219 isopleths of grossular.

Fig. 11. Representative fits for the measured and calculated (diffusion model) almandine and pyrope profiles from sample (a) WG1 and (b) WG336.

Fig. 12. PT paths reported for the Moldanubian granulites (modified after Jedlička et al., 2015). 1 - Kutná Hora (Perraki and Faryad, 2014; Jedlička et al., 2015), 2 - Strážek Unit (Tajčmanová et al., 2009), 3 - Blanský les and Lišov (Vrána, 1992; Kotková and Harley, 1999, 2010), 4 – Dunkelsteinerwald and St. Leonhard (Carswell and O'Brien, 1993; O'Brien and Rötzler, 2003), 5 - St. Leonhard (Cooke, 2000; Cooke et al. 2000).

Fig. 13. Reconstructed PT paths and estimated exhumation and cooling rates for the Moldanubian granulites in the southeastern Bohemian Massif. Field a and b indicates estimated PT conditions for the formation of the metamorphic peak and the retrograde mineral assemblage, respectively. Peritectic garnet growth reactions (1) bt + als + qz = ms + grt + melt, (2) bt + ms + qz = grt + kfs + melt, (3) ms + qz = grt + kfs + als + melt, (4) bt + als + qz = grt + kfs + melt (5) ms + cpx + qz = grt + kfs + melt are from Vielzeuf and Holloway (1988) and Patiño Douce (2005). Biotite stability is from Hermann (2002).

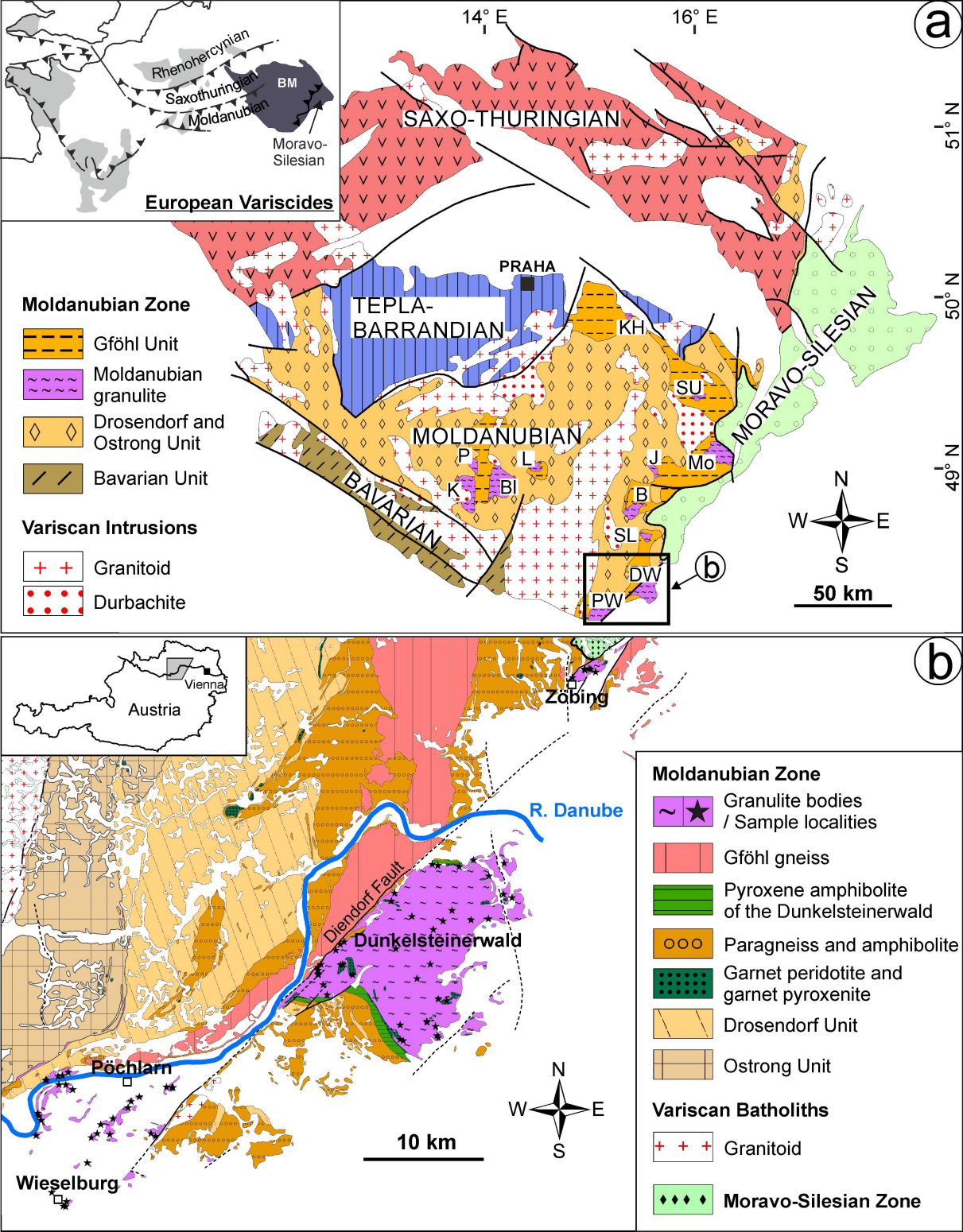
a
14° E
16° E
51° N
50° N
49° N
Rhenohercynian
Saxothuringian
Moldanubian
BM
Moravo-Silesian
European Variscides
SAXO-THURINGIAN
PRAHA
TEPLA-BARRANDIAN
MOLDANUBIAN
BAVARIAN
MORAVO-SILESIAN
KH
SU
P
L
J
Mo
K
Bl
B
SL
DW
PW
b
N
W
E
S
50 km
Moldanubian Zone
Gföhl Unit
Moldanubian granulite
Drosendorf and Ostrong Unit
Bavarian Unit
Variscan Intrusions
Granitoid
Durbachite
b
Vienna
Austria
Zöbing
R. Danube
Diendorf Fault
Dunkelsteinerwald
Pöchlarn
Wieselburg
10 km
Moldanubian Zone
Granulite bodies / Sample localities
Gföhl gneiss
Pyroxene amphibolite of the Dunkelsteinerwald
Paragneiss and amphibolite
Garnet peridotite and garnet pyroxenite
Drosendorf Unit
Ostrong Unit
Variscan Batholiths
Granitoid
Moravo-Silesian Zone

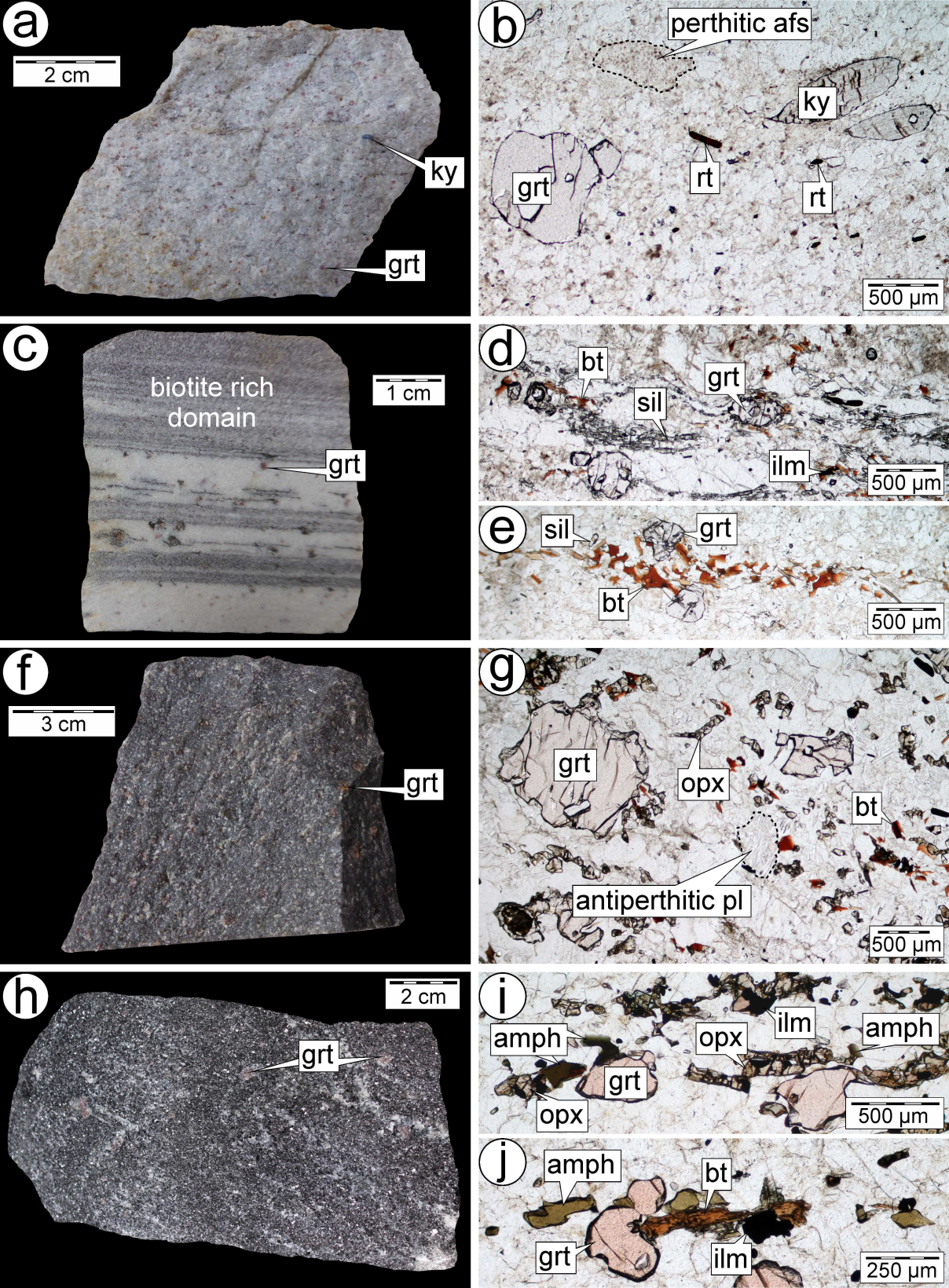
a
2 cm
ky
grt
b
perthitic afs
ky
grt
rt
rt
500 µm
c
biotite rich
domain
1 cm
grt
d
bt
grt
sil
ilm
500 µm
e
sil
grt
bt
500 µm
f
3 cm
grt
g
grt
opx
bt
antiperthitic pl
500 µm
h
2 cm
grt
i
amph
ilm
opx
amph
grt
opx
500 µm
j
amph
bt
grt
ilm
250 µm

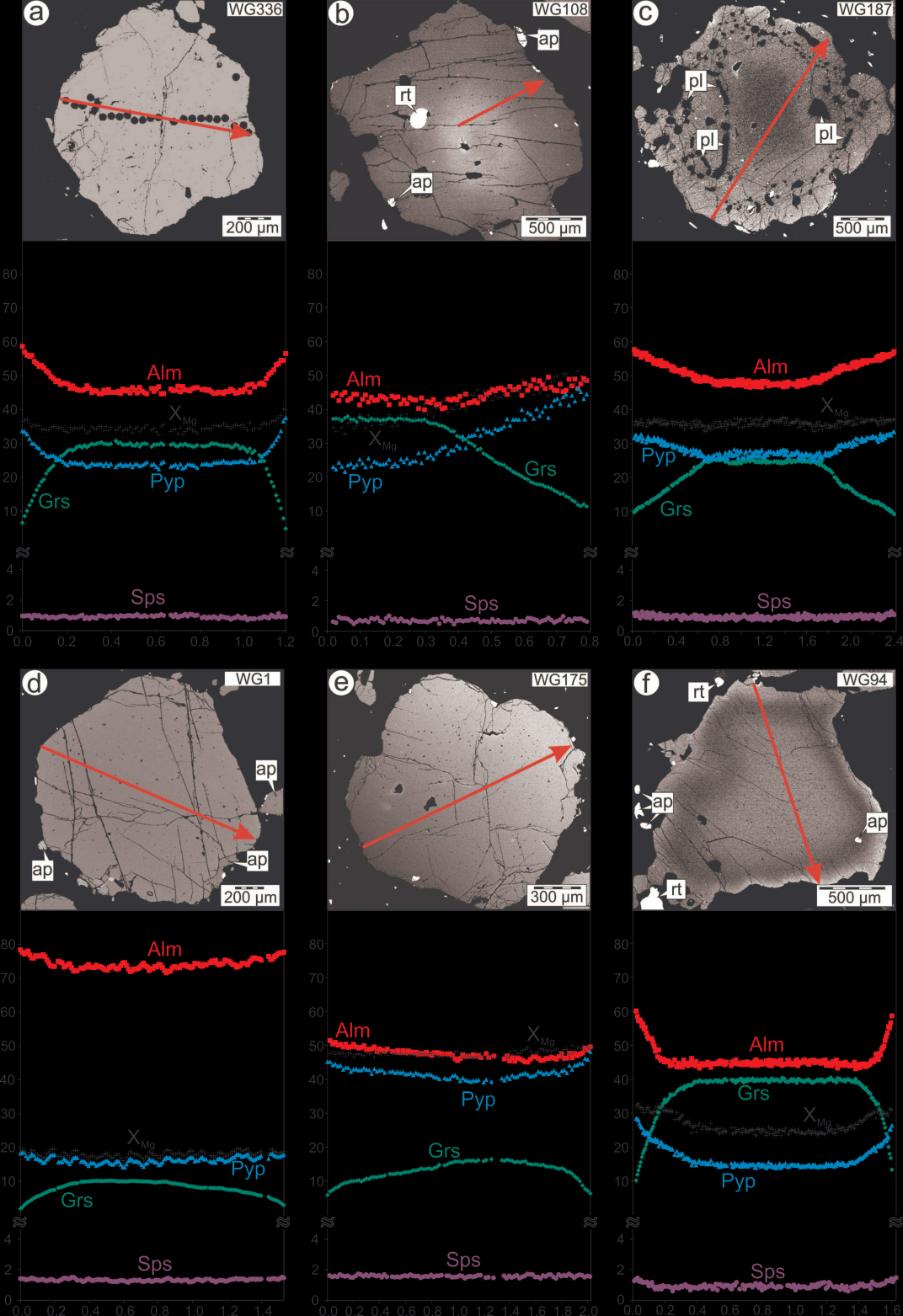
a
WG336
200 µm
b
WG108
ap
rt
ap
500 µm
c
WG187
pl
pl
pl
500 µm
Alm
X_{Mg}
Pyp
Grs
Sps
d
WG1
ap
ap
ap
200 µm
e
WG175
300 µm
f
WG94
rt
ap
ap
rt
500 µm

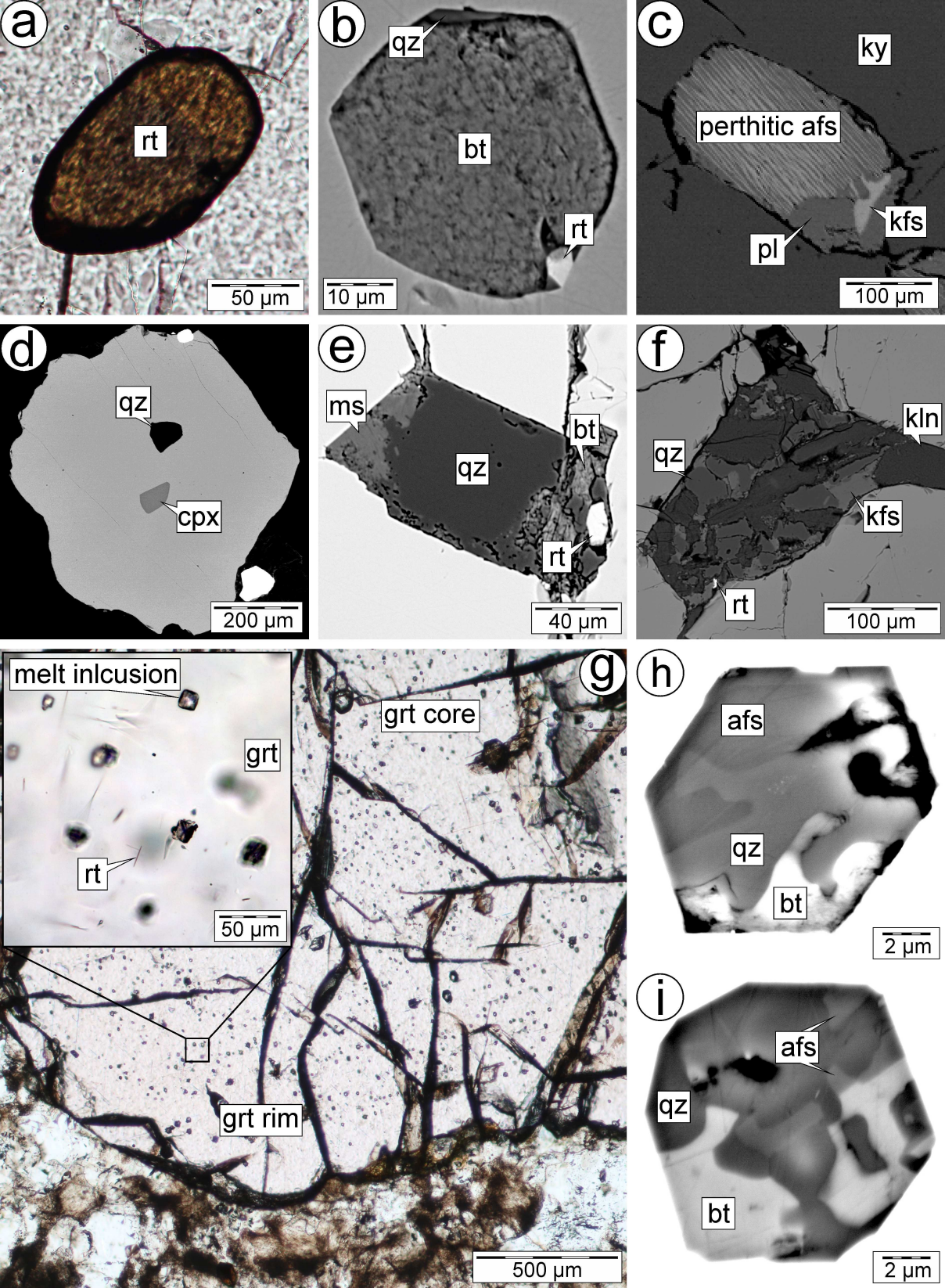
a
rt
50 µm
b
qz
bt
rt
10 µm
c
ky
perthitic afs
kfs
pl
100 µm
d
qz
cpx
200 µm
e
ms
qz
bt
rt
40 µm
f
kln
qz
kfs
rt
100 µm
melt inlcusion
grt
rt
50 µm
g
grt core
grt rim
500 µm
h
afs
qz
bt
2 µm
i
afs
qz
bt
2 µm

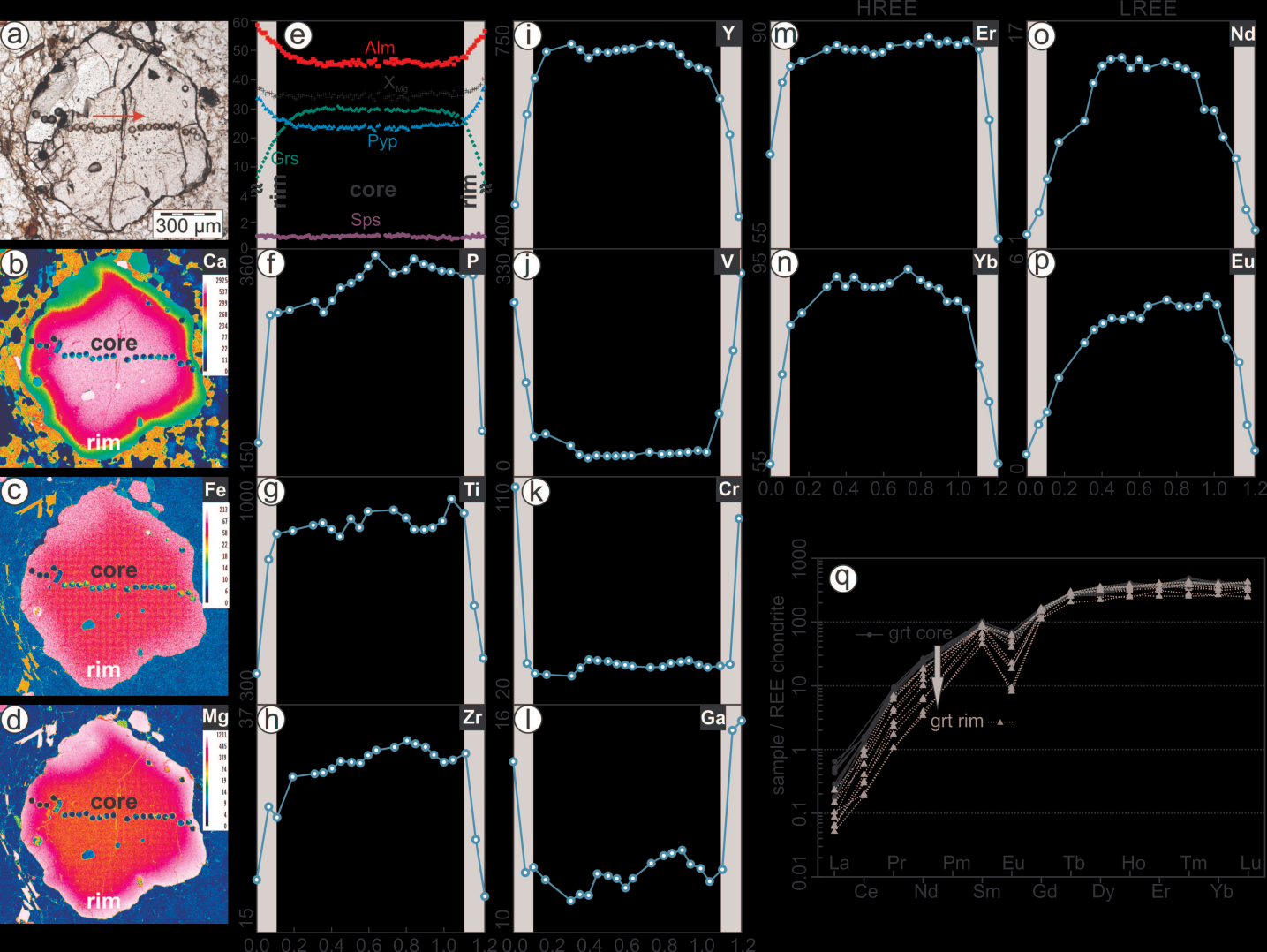
a
300 µm
b
Ca
core
rim
c
Fe
core
rim
d
Mg
core
rim
e
Alm
X_{Mg}
Pyp
Grs
Sps
rim
core
rim
f
P
g
Ti
h
Zr
i
Y
j
V
k
Cr
l
Ga
HREE
LREE
m
Er
n
Yb
o
Nd
p
Eu
0.0 0.2 0.4 0.6 0.8 1.0 1.2
q
grt core
grt rim
sample / REE chondrite
La Ce Pr Nd Pm Sm Eu Gd Tb Dy Ho Er Tm Yb Lu

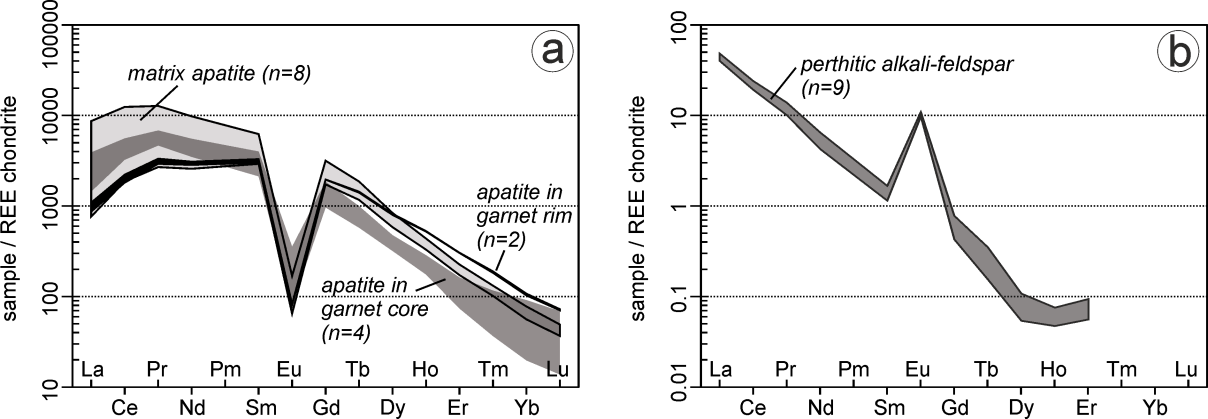
a
matrix apatite (n=8)
apatite in garnet rim (n=2)
apatite in garnet core (n=4)
sample / REE chondrite
100000
10000
1000
100
10
La
Ce
Pr
Nd
Pm
Sm
Eu
Gd
Tb
Dy
Ho
Er
Tm
Yb
Lu
b
perthitic alkali-feldspar (n=9)
sample / REE chondrite
100
10
1
0.1
0.01

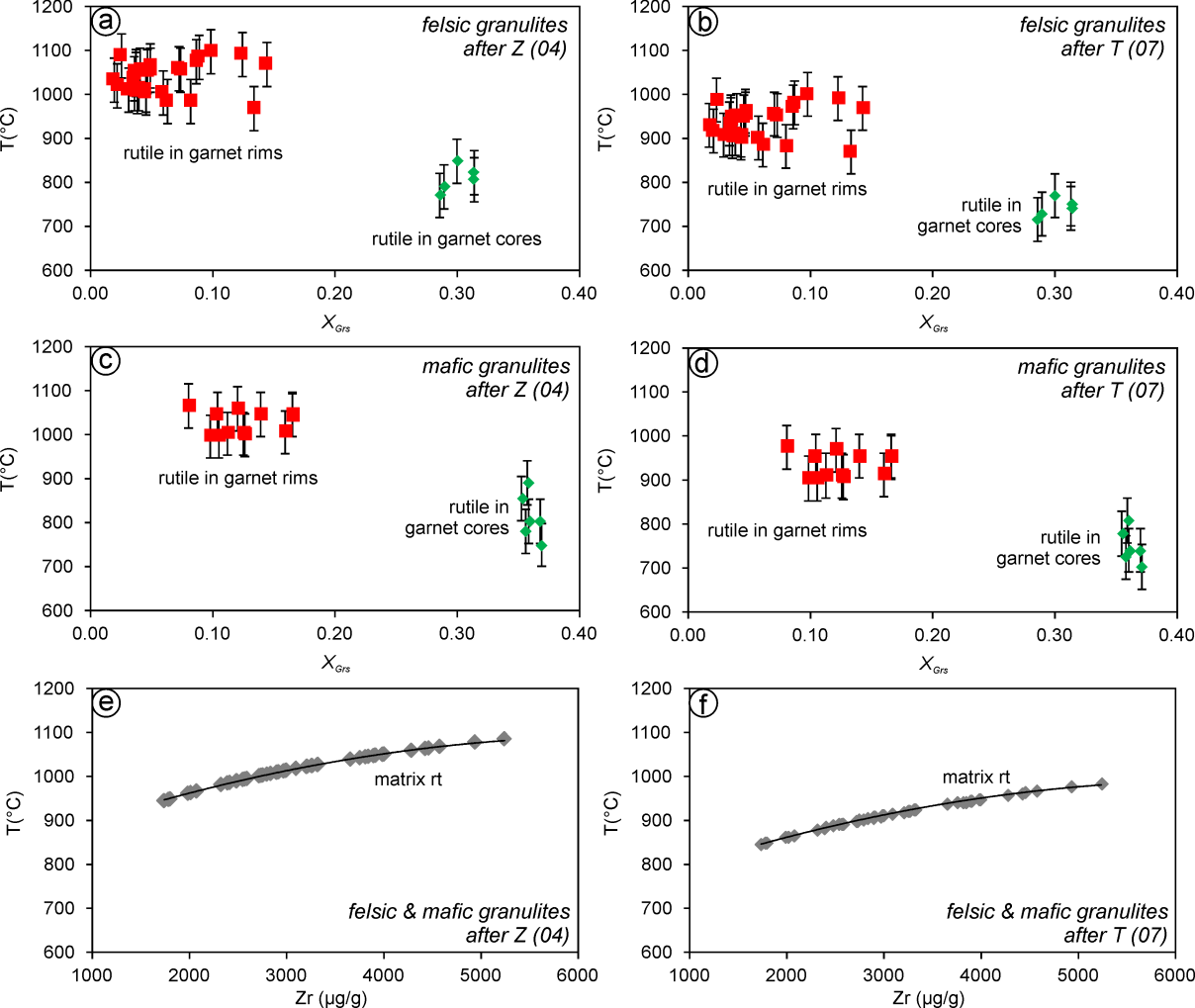
a
felsic granulites
after Z (04)
rutile in garnet rims
rutile in garnet cores
T(°C)
X_{Grs}
b
felsic granulites
after T (07)
rutile in garnet rims
rutile in
garnet cores
c
mafic granulites
after Z (04)
rutile in garnet rims
rutile in
garnet cores
d
mafic granulites
after T (07)
rutile in garnet rims
rutile in
garnet cores
e
matrix rt
felsic & mafic granulites
after Z (04)
Zr (µg/g)
f
matrix rt
felsic & mafic granulites
after T (07)
Zr (µg/g)

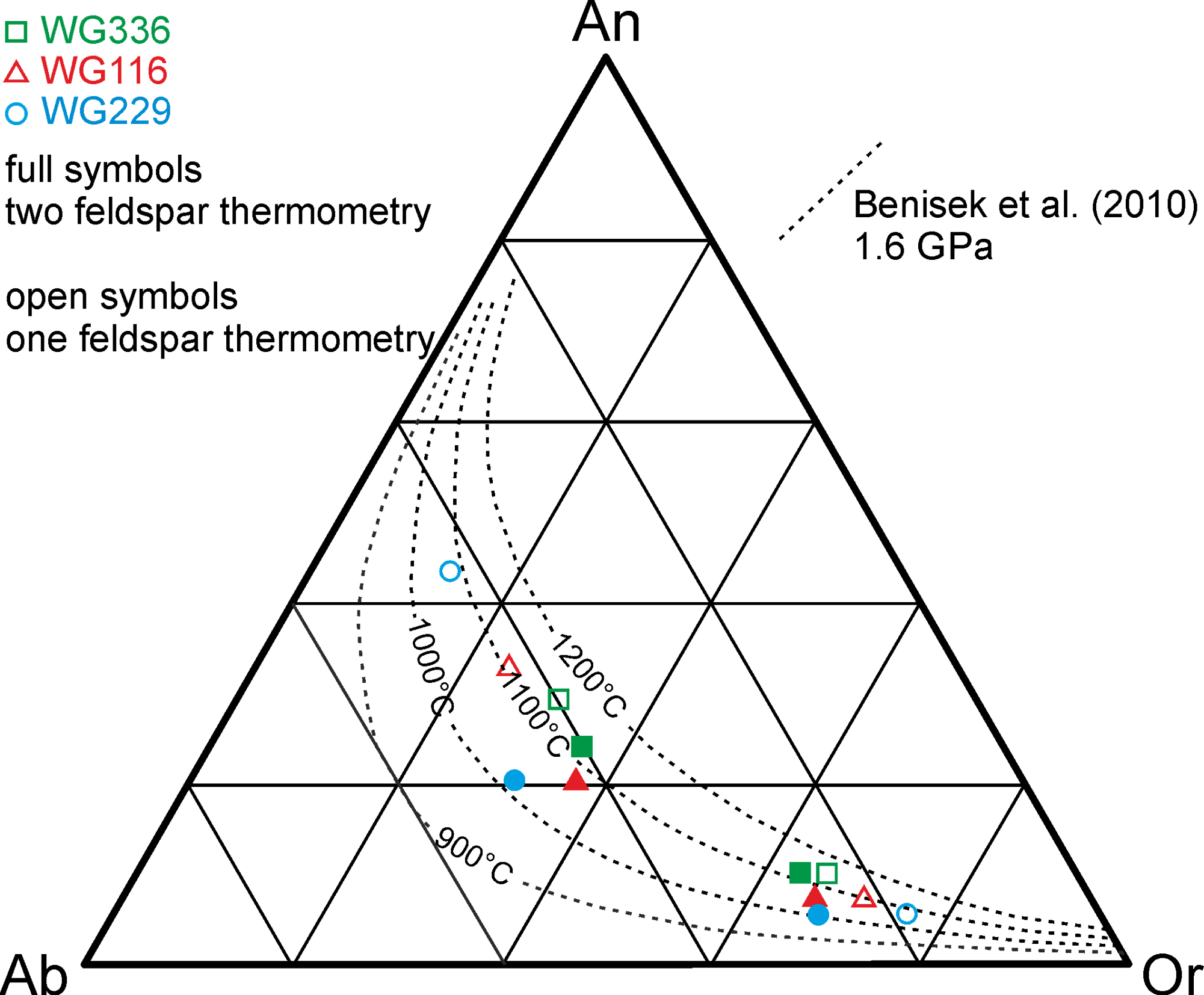
WG336
WG116
WG229
full symbols
two feldspar thermometry
open symbols
one feldspar thermometry
An
Ab
Or
Benisek et al. (2010)
1.6 GPa
1000°C
1100°C
1200°C
900°C

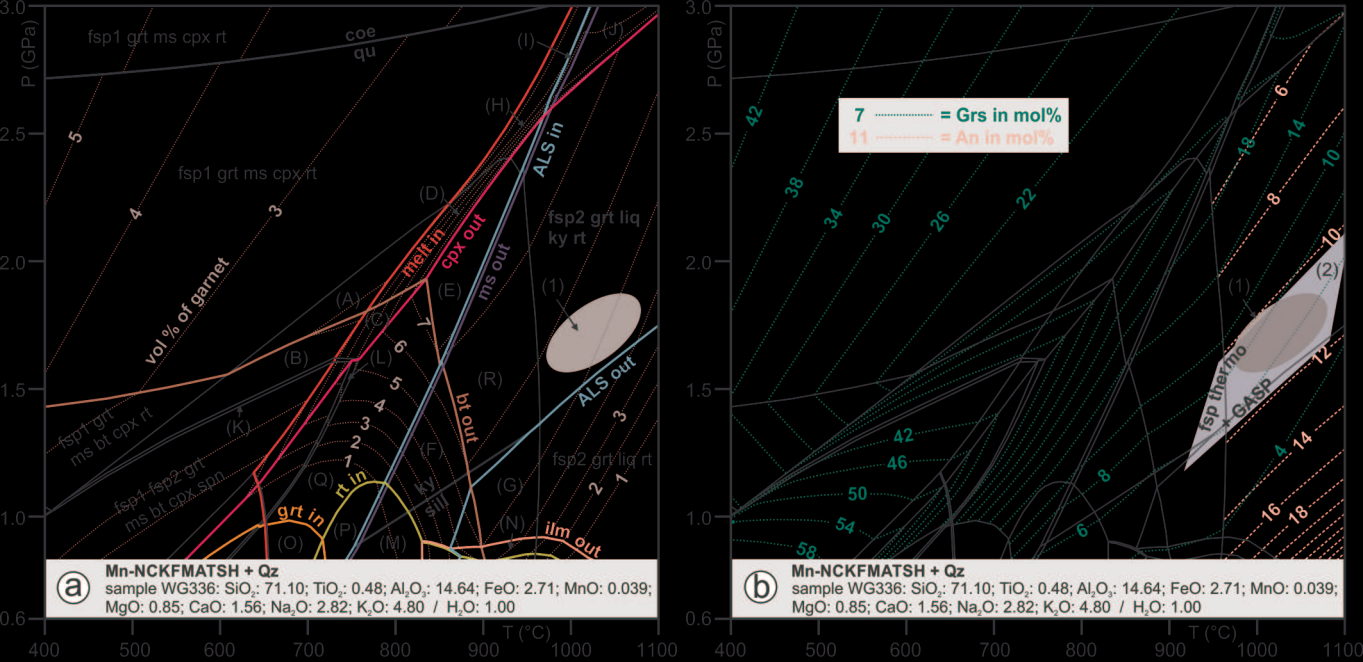

(A) fsp1 fsp2 grt ms cpx rt
(B) fsp1 fsp 2 grt ms bt cpx rt
(C) fsp1 fsp 2 grt ms bt cpx liq rt
(D) fsp1 fsp2 grt ms cpx liq rt
(E) fsp1 fsp2 grt ms liq rt
(F) fsp1 fsp2 bt grt liq ky rt
(G) fsp1 fsp2 grt liq rt
(H) fsp1 grt ms cpx liq rt
(I) fsp1 grt ms cpx liq ky rt
(J) fsp1 grt cpx liq ky rt
(K) fsp1 fsp2 grt ms bt cpx rt spn
(L) fsp1 fsp2 grt ms bt liq rt spn
(M) fsp1 fsp2 bt liq sill
(N) fsp1 fsp2 grt liq rt ilm
(O) fsp1 fsp2 ms bt liq rt
(P) fsp1 fsp2 ms grt bt liq
(Q) fsp1 fsp2 ms grt bt liq rt
(R) fsp1 fsp2 grt liq ky rt

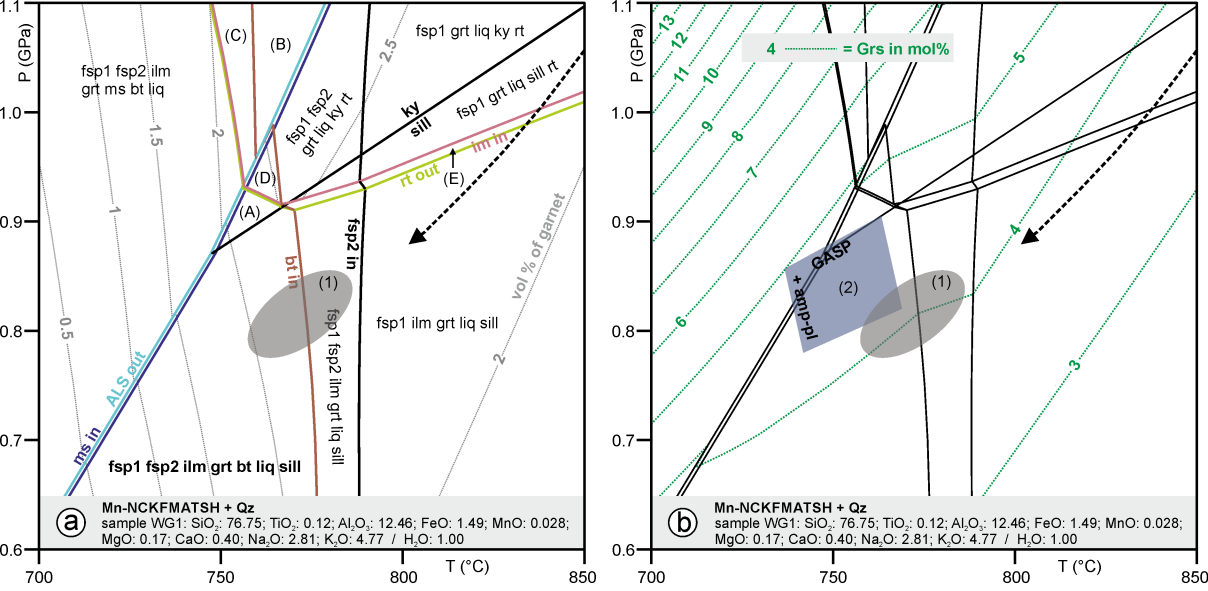

(A) fsp1 fsp2 ilm grt bt liq ky (B) fsp1 fsp 2 grt ms liq rt (C) fsp1 fsp 2 grt ms bt liq rt (D) fsp1 fsp2 grt bt liq ky rt (E) fsp1 ilm grt liq sill rt

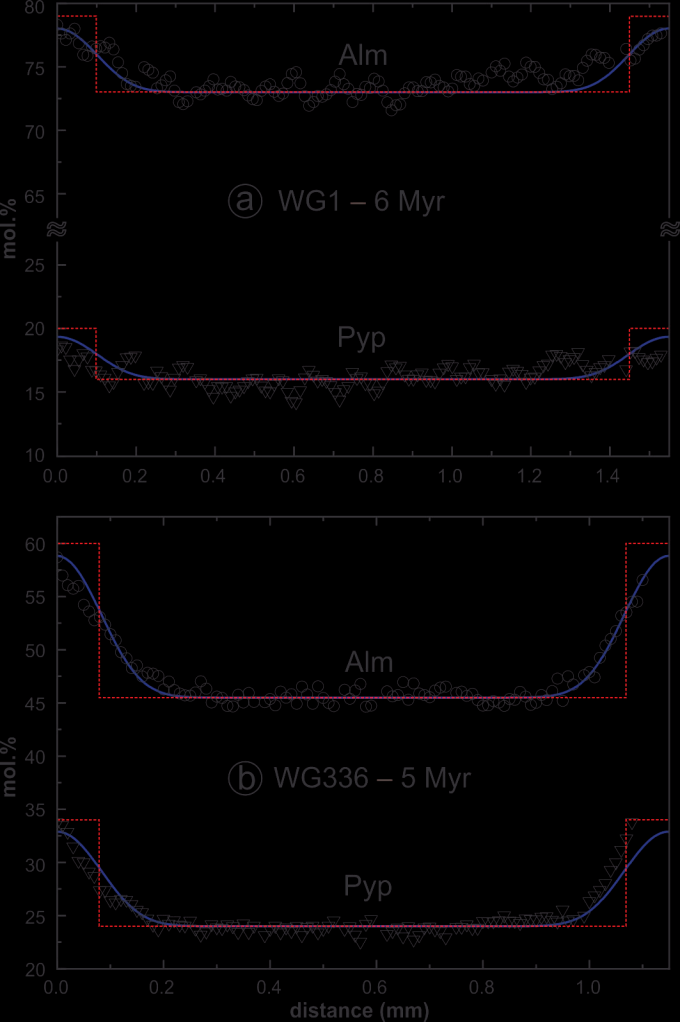
Alm
ⓐ WG1 – 6 Myr
Pyp
mol.%
Alm
ⓑ WG336 – 5 Myr
Pyp
mol.%
distance (mm)

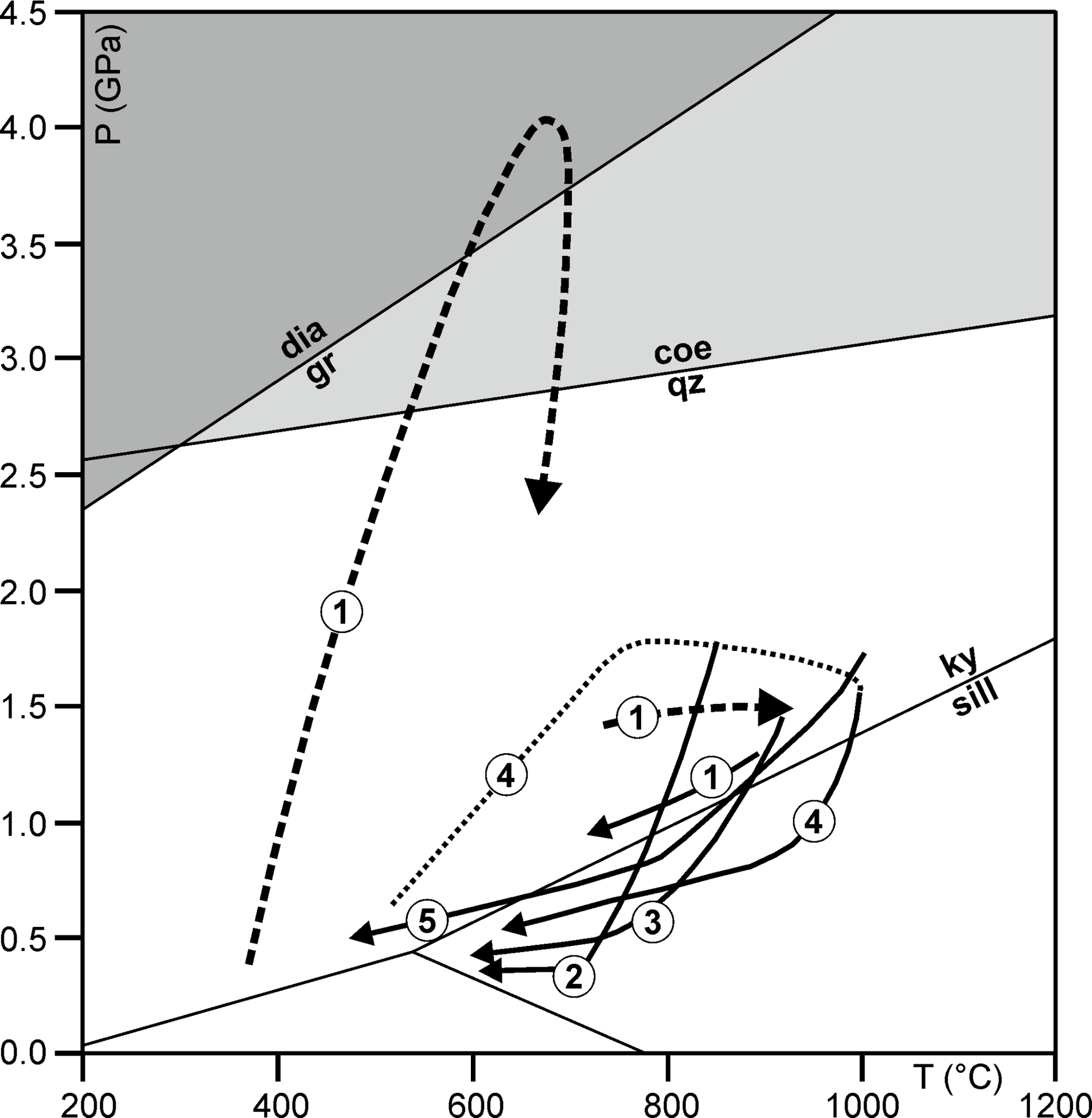
P (GPa)
4.5
4.0
3.5
3.0
2.5
2.0
1.5
1.0
0.5
0.0
dia
gr
coe
qz
ky
sill
1
1
4
1
4
5
3
2
T (°C)
200
400
600
800
1000
1200

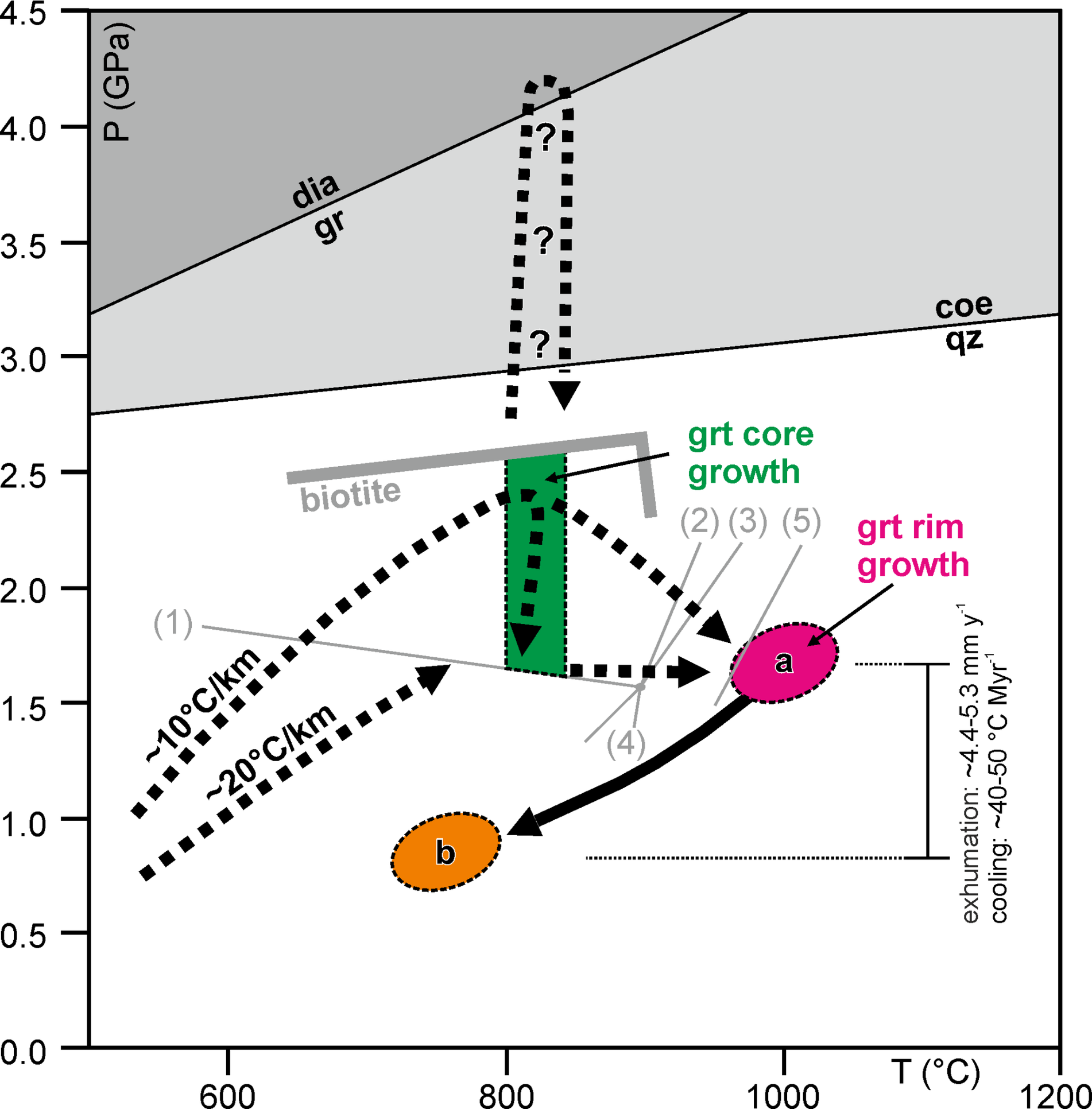
P (GPa)
4.5
4.0
3.5
3.0
2.5
2.0
1.5
1.0
0.5
0.0
dia
gr
coe
qz
?
?
?
biotite
grt core
growth
grt rim
growth
(1)
(2)
(3)
(4)
(5)
~10°C/km
~20°C/km
a
b
exhumation: ~4.4-5.3 mm y-1
cooling: ~40-50 °C Myr-1
600
800
1000
1200
T (°C)

Table 1 Representative composition of garnet and clinopyroxene inclusions in garnet.

Mineral	garnet																				cpx	
Rock type	felsic granulite												mafic granulite									
Sample WG	1				108		175		187		336		93		94		342		345		344	
Location*	r	c	#	#	r	c	r	c	r	c	r	c	r	r	r	c	r	r	r	r	inc	
SiO_2 wt.%	36.90	36.63	36.83	37.03	39.15	38.29	38.54	37.72	38.91	38.85	37.76	38.15	36.19	37.54	38.00	38.54	37.30	37.78	36.38	37.05	51.71	51.78
TiO_2	0.11	0.13	b.d.	0.13	0.03	0.21	b.d.	0.12	0.16	0.16	b.d.	0.19	b.d.	b.d.	b.d.	b.d.	b.d.	0.22	b.d.	b.d.	0.21	0.34
Al_2O_3	21.21	21.66	21.04	21.66	22.04	22.26	22.45	22.50	22.48	23.18	22.11	21.87	20.64	21.02	21.60	21.46	20.56	21.24	20.96	20.96	1.84	1.71
Cr_2O_3	b.d.	0.10	0.06	b.d.	0.06	0.06	0.05	0.00	0.15	0.09	b.d.	b.d.	b.d.	b.d.	b.d.	b.d.	0.07	b.d.	b.d.	b.d.	b.d.	b.d.
FeO	35.19	33.33	34.72	34.89	23.95	20.02	24.99	23.62	25.84	21.64	28.01	22.59	34.94	28.37	27.96	21.09	30.91	25.62	30.98	30.69	14.70	12.94
MnO	0.57	0.46	0.63	0.57	0.39	0.35	0.72	0.67	0.56	0.38	0.43	0.42	1.33	0.73	0.59	0.45	0.98	0.59	1.06	1.00	0.07	0.16
MgO	4.09	4.05	4.28	4.29	10.79	5.70	11.39	9.77	8.34	6.98	8.52	6.07	3.06	2.56	7.54	4.64	4.16	4.57	4.62	4.75	10.22	11.13
CaO	1.38	3.44	1.40	1.43	3.79	12.82	1.72	4.95	3.63	8.62	2.32	10.63	2.61	9.51	3.62	13.34	5.88	10.30	5.39	5.62	19.79	20.57
Na_2O	b.d.	b.d.	b.d.	b.d.	b.d.	b.d.	b.d.	b.d.	b.d.	b.d.	b.d.	b.d.	b.d.	b.d.	b.d.	b.d.	b.d.	b.d.	b.d.	b.d.	0.52	0.53
Total	**99.45**	**99.80**	**98.96**	**100.00**	**100.20**	**99.71**	**99.86**	**99.35**	**100.07**	**99.90**	**99.15**	**99.92**	**98.77**	**99.73**	**99.31**	**99.61**	**99.86**	**100.32**	**99.39**	**100.07**	**99.06**	**99.16**
	atoms per 12 O																				*atoms per 6 O*	
Si	2.968	2.921	2.972	2.954	2.963	2.945	2.926	2.887	2.986	2.968	2.939	2.942	2.948	2.983	2.967	2.990	2.961	2.941	2.894	2.924	1.985	1.976
Ti	0.007	0.008	0.002	0.008	0.002	0.012	0.000	0.007	0.009	0.009	0.000	0.011	0.000	0.000	0.000	0.005	0.000	0.013	0.000	0.000	0.006	0.010
Al	2.010	2.036	2.001	2.037	1.966	2.018	2.009	2.030	2.033	2.087	2.028	1.987	1.981	1.969	1.988	1.962	1.924	1.949	1.965	1.950	0.083	0.077
Cr	0.000	0.006	0.004	0.002	0.004	0.004	0.003	0.000	0.009	0.005	0.000	0.000	0.000	0.000	0.000	0.000	0.004	0.000	0.000	0.000	0.000	0.000
Fe^{3+}	0.041	0.100	0.048	0.037	0.101	0.063	0.136	0.182	0.000	0.000	0.095	0.107	0.123	0.064	0.078	0.048	0.149	0.142	0.246	1.823	0.000	0.000
Fe^{2+}	2.326	2.122	2.295	2.291	1.415	1.224	1.451	1.330	1.658	1.382	1.728	1.349	2.257	1.821	1.748	1.320	1.903	1.526	1.816	0.203	0.472	0.413
Mn	0.039	0.031	0.043	0.039	0.025	0.023	0.046	0.043	0.036	0.025	0.028	0.027	0.092	0.049	0.039	0.030	0.066	0.039	0.071	0.067	0.002	0.005
Mg	0.490	0.481	0.515	0.510	1.217	0.654	1.289	1.115	0.954	0.795	0.989	0.698	0.372	0.303	0.878	0.537	0.492	0.530	0.548	0.559	0.585	0.633
Ca	0.119	0.294	0.121	0.122	0.307	1.057	0.140	0.406	0.298	0.706	0.193	0.878	0.228	0.810	0.303	1.109	0.500	0.859	0.459	0.475	0.814	0.841
Na																					0.039	0.039
Σ Cat.	**8.000**	**7.999**	**8.001**	**8.000**	**8.000**	**8.000**	**8.000**	**8.000**	**7.984**	**7.977**	**8.000**	**7.999**	**8.000**	**8.000**	**8.000**	**8.000**	**8.000**	**8.000**	**8.000**	**8.000**	**3.986**	**3.995**
Alm *mol%*	78.2	72.5	77.2	77.3	47.7	41.4	49.6	46.0	56.3	47.5	58.8	45.7	76.6	61.0	58.9	44.1	64.3	51.6	62.7	62.3		
Pyp	16.5	16.4	17.3	17.2	41.1	22.1	44.1	38.5	32.4	27.3	33.6	23.6	12.6	10.2	29.6	17.9	16.6	18.0	18.9	19.1		
Grs	4.0	10.0	4.1	4.1	10.4	35.7	4.8	14.0	10.1	24.3	6.6	29.7	7.7	27.1	10.2	37.0	16.9	29.1	15.9	16.3		
Sps	1.3	1.1	1.4	1.3	0.8	0.8	1.6	1.5	1.2	0.8	1.0	0.9	3.1	1.6	1.3	1.0	2.2	1.3	2.5	2.3		
X_{Mg}	0.174	0.185	0.183	0.182	0.462	0.348	0.470	0.456	0.365	0.365	0.364	0.341	0.141	0.143	0.334	0.289	0.205	0.258	0.232	0.734	0.553	0.605
X_{Na}																					0.046	0.044
Al^{IV}																					0.015	0.024

*specifies textural position of analyzed mineral: r-rim; c-core; #-garnet in biotite and sillimanite rich domains; inc-inclusion in garnet

Table 2 Representative composition of muscovite, biotite, orthopyroxene and amphibole.

Mineral	muscovite		biotite			orthopyroxene		amphibole	
Rock type	felsic	mafic	felsic granulite		mafic granulite				
Sample WG	336	344	4	178	345	87	342	345	
Location*	inc	inc	mx	inc	mx	core	rim	rim	core
SiO_2 wt.%	46.90	47.57	38.60	38.18	35.87	48.00	49.88	39.89	40.24
TiO_2	b.d.	b.d.	1.62	6.13	4.34	0.10	0.11	2.26	2.02
Al_2O_3	32.75	37.43	15.37	15.39	15.38	0.44	1.19	11.65	10.80
Cr_2O_3	b.d.	b.d.	0.06	b.d.	b.d.	b.d.	b.d.	b.d.	b.d.
FeO	2.47	1.68	13.57	8.46	21.26	43.06	33.78	20.44	20.20
MnO	0.00	b.d.	b.d.	b.d.	b.d.	0.42	0.43	0.12	0.14
MgO	1.44	0.90	16.02	17.21	9.50	6.80	14.21	7.45	8.06
CaO	0.05	b.d.	b.d.	b.d.	0.05	1.06	0.57	10.95	10.91
Na_2O	0.26	0.94	0.07	0.25	b.d.	b.d.	b.d.	1.70	1.56
K_2O	10.73	9.97	9.94	9.91	9.38			1.86	1.75
F	0.43	b.d.	5.40	2.32	0.48			0.06	0.05
Cl	b.d.	b.d.	b.d.	0.09	0.05			0.35	0.35
Total	**95.03**	**98.49**	**100.65**	**97.94**	**96.31**	**99.88**	**100.17**	**96.73**	**96.08**
	atoms per 11 O					*atoms per 6 O*		*atoms per 23 O*	
Si	3.164	3.054	2.859	2.762	2.751	1.992	1.960	6.229	6.302
Ti	0.000	0.000	0.090	0.333	0.250	0.003	0.003	0.265	0.238
Al^{IV}	0.836	0.946	1.141	1.238	1.249	0.008	0.040	1.771	1.698
Al^{VI}	1.768	1.886	0.201	0.073	0.141	0.014	0.016	0.373	0.295
Cr	0.000	0.000	0.004	0.000	0.000	0.000	0.000	0.000	0.000
Fe^{3+}	0.000	0.000	0.000	0.000	0.000	0.000	0.018	0.203	0.284
Fe^{2+}	0.139	0.090	0.841	0.512	1.364	1.494	1.093	2.467	2.361
Mn	0.000	0.000	0.000	0.000	0.000	0.015	0.014	0.016	0.019
Mg	0.145	0.086	1.769	1.856	1.086	0.421	0.833	1.734	1.882
Ca	0.004	0.000	0.000	0.000	0.004	0.047	0.024	1.832	1.831
Na	0.034	0.117	0.010	0.035	0.000	0.000	0.000	0.515	0.474
K	0.923	0.817	0.939	0.914	0.918			0.371	0.350
F	0.092	0.000	1.265	0.531	0.116			0.030	0.025
Cl	0.000	0.000	0.000	0.011	0.006			0.093	0.093
Σ Cat.	**7.013**	**6.996**	**7.853**	**7.724**	**7.763**	**3.994**	**4.001**	**15.775**	**15.734**
X_{Mg}	0.511	0.489	0.678	0.784	0.443	0.220	0.433	0.413	0.444

*specifies textural position of analyzed mineral: inc-inclusion in garnet; mx-matrix;

Table 3 Representative composition of former ternary feldspar and K-feldspar.

Mineral	former ternary feldspar										kfs
Rock type	felsic granulite								mafic granulite		
Sample WG	116		329		336		192		94		345
Location*	ho	ex	ho	ex	ho	ex	ho #	ex #	ex	ho	mx
SiO_2 wt.%	64.57	62.95	65.21	63.07	64.96	62.49	65.29	65.27	66.11	58.98	64.40
Al_2O_3	19.01	22.57	18.77	22.75	18.78	23.30	18.01	22.23	18.01	26.17	18.91
CaO	0.12	4.29	0.05	3.93	0.12	4.76	b.d.	2.76	b.d.	7.94	0.09
BaO	0.17	b.d.	b.d.	b.d.	0.14	b.d.	b.d.	b.d.	b.d.	b.d.	0.58
Na_2O	1.05	9.01	1.10	9.08	1.29	8.91	1.15	9.93	0.73	6.94	0.95
K_2O	15.44	0.26	15.27	0.67	14.86	0.18	15.31	0.13	15.14	0.27	15.23
Total	**100.36**	**99.08**	**100.40**	**99.50**	**100.15**	**99.64**	**99.76**	**100.32**	**99.99**	**100.30**	**100.16**
Si *per 8 O*	2.971	2.806	2.987	2.805	2.985	2.777	3.014	2.858	3.025	2.615	2.974
Al	1.031	1.186	1.013	1.192	1.017	1.220	0.980	1.152	0.971	1.368	1.029
Ca	0.006	0.205	0.002	0.187	0.006	0.227	0.000	0.129	0.000	0.377	0.004
Ba	0.003	0.000	0.000	0.000	0.003	0.000	0.000	0.000	0.000	0.000	0.010
Na	0.094	0.779	0.098	0.783	0.115	0.768	0.103	0.843	0.065	0.597	0.085
K	0.906	0.015	0.892	0.038	0.871	0.010	0.902	0.007	0.884	0.015	0.897
Σ Cat.	**5.011**	**4.991**	**4.992**	**5.005**	**4.997**	**5.001**	**4.999**	**4.989**	**4.945**	**4.972**	**4.999**
An *mol%*	0.6	20.5	0.2	18.6	0.6	22.6	0.0	13.2	0.0	38.1	0.4
Ab	9.3	78.0	9.9	77.7	11.6	76.4	10.2	86.1	6.8	60.4	8.6
Or	90.1	1.5	89.9	3.8	87.8	1.0	89.8	0.7	93.2	1.5	91.0
	reintegrated		reintegrated		reintegrated		reintegrated		reintegrated		
An *mol%*	8.5		4.9		11.0		5.9		38.9		
Ab	21.4		16.9		25.2		25.8		34.6		
Or	70.2		78.2		63.8		68.4		26.4		

*specifies textural position of analyzed mineral: ho-host; ex-exsolution; #-feldspar enclosed in kyanite

Table 4 Representative composition of plagioclase.

Mineral	plagioclase				
Rock type	felsic granulite			mafic granulite	
Sample WG	116	322	336	87	345
Location*	mx	mx	mx	mx	mx
SiO_2 wt.%	63.40	64.14	62.46	61.04	61.53
Al_2O_3	22.88	22.66	23.34	23.98	23.65
CaO	4.32	3.51	5.01	5.73	5.58
BaO	b.d.	b.d.	b.d.	b.d.	b.d.
Na_2O	8.89	9.15	8.54	8.15	8.22
K_2O	0.26	0.50	0.24	0.48	0.35
Total	**99.75**	**99.96**	**99.59**	**99.38**	**99.33**
Si *per 8 O*	2.803	2.828	2.775	2.725	2.747
Al	1.192	1.178	1.222	1.262	1.245
Ca	0.205	0.166	0.238	0.274	0.267
Ba	0.000	0.000	0.000	0.000	0.000
Na	0.762	0.782	0.736	0.705	0.712
K	0.015	0.028	0.014	0.027	0.020
Σ Cat.	**4.977**	**4.982**	**4.985**	**4.993**	**4.991**
An *mol%*	20.9	17.0	24.1	27.2	26.7
Ab	77.6	80.1	74.5	70.1	71.3
Or	1.5	2.9	1.4	2.7	2.0

*specifies textural pos. of analyzed mineral: mx-matrix